

Global radiative forcing of coupled tropospheric ozone and aerosols in a unified general circulation model

Hong Liao and John H. Seinfeld

Division of Engineering and Applied Science and Department of Chemical Engineering, California Institute of Technology, Pasadena, California, USA

Peter J. Adams

Department of Civil and Environmental Engineering and Department of Engineering and Public Policy, Carnegie Mellon University, Pittsburgh, Pennsylvania, USA

Loretta J. Mickley

Department of Earth and Planetary Sciences and Division of Engineering and Applied Sciences, Harvard University, Cambridge, Massachusetts, USA

Received 16 December 2003; revised 30 March 2004; accepted 14 June 2004; published 21 August 2004.

[1] Global simulations of sea salt and mineral dust aerosols are integrated into a previously developed unified general circulation model (GCM), the Goddard Institute for Space Studies (GISS) GCM II', that simulates coupled tropospheric ozone-NO_x-hydrocarbon chemistry and sulfate, nitrate, ammonium, black carbon, primary organic carbon, and secondary organic carbon aerosols. The fully coupled gas-aerosol unified GCM allows one to evaluate the extent to which global burdens, radiative forcing, and eventually climate feedbacks of ozone and aerosols are influenced by gas-aerosol chemical interactions. Estimated present-day global burdens of sea salt and mineral dust are 6.93 and 18.1 Tg with lifetimes of 0.4 and 3.9 days, respectively. The GCM is applied to estimate current top of atmosphere (TOA) and surface radiative forcing by tropospheric ozone and all natural and anthropogenic aerosol components. The global annual mean value of the radiative forcing by tropospheric ozone is estimated to be +0.53 W m⁻² at TOA and +0.07 W m⁻² at the Earth's surface. Global, annual average TOA and surface radiative forcing by all aerosols are estimated as -0.72 and -4.04 W m⁻², respectively. While the predicted highest aerosol cooling and heating at TOA are -10 and +12 W m⁻², respectively, surface forcing can reach values as high as -30 W m⁻², mainly caused by the absorption by black carbon, mineral dust, and OC. We also estimate the effects of chemistry-aerosol coupling on forcing estimates based on currently available understanding of heterogeneous reactions on aerosols. Through altering the burdens of sulfate, nitrate, and ozone, heterogeneous reactions are predicted to change the global mean TOA forcing of aerosols by 17% and influence global mean TOA forcing of tropospheric ozone by 15%.

INDEX TERMS: 0305 Atmospheric Composition and Structure: Aerosols and particles (0345, 4801); 0345 Atmospheric Composition and Structure: Pollution—urban and regional (0305); 0365 Atmospheric Composition and Structure: Troposphere—composition and chemistry; **KEYWORDS:** radiative forcing, mineral dust, sea salt

Citation: Liao, H., J. H. Seinfeld, P. J. Adams, and L. J. Mickley (2004), Global radiative forcing of coupled tropospheric ozone and aerosols in a unified general circulation model, *J. Geophys. Res.*, 109, D16207, doi:10.1029/2003JD004456.

1. Introduction

[2] To date, a large number of studies have focused on the global distribution and radiative forcing of tropospheric ozone [Chalita et al., 1996; van Dorland et al., 1997; Stevenson et al., 1998; Mickley et al., 1999; Roelofs and Lelieveld, 2000; Berntsen et al., 2000; Hauglustaine and Brasseur, 2001; Shindell et al., 2001], sulfate [Boucher

and Anderson, 1995; Feichter et al., 1997; Penner et al., 1998; Koch et al., 1999; Kiehl et al., 2000; Adams et al., 2001], carbonaceous aerosols [Schult et al., 1997; Penner et al., 1998; Cooke et al., 1999; Jacobson, 2000; Koch, 2001; Chung and Seinfeld, 2002], sea salt [Gong et al., 1997; Jacobson, 2001; Grini et al., 2002; Takemura et al., 2002], and mineral dust [Tegen and Lacis, 1996; Woodward, 2001; Jacobson, 2001; Takemura et al., 2002], but only a few have examined the combined direct radiative forcing of all these major classes of aerosols [Ghan et al., 2001; Jacobson, 2001; Takemura et al., 2002].

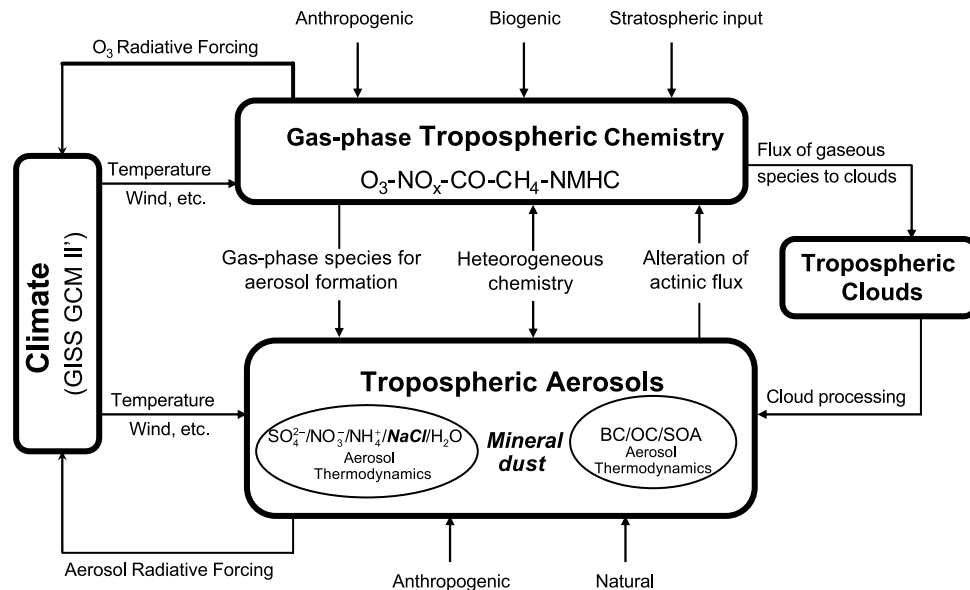


Figure 1. Structure of the GCM-atmospheric chemistry-aerosol-climate coupled model. See text for the details for the chemistry-aerosol interactions.

[3] The processes that determine the levels of tropospheric gas-phase species and aerosols are coupled. Gas-phase chemistry influences the formation and growth of aerosols. For example, sulfate formation depends on the gas-phase concentrations of OH, NO₃, HO₂, and O₃. Nitrogen oxides (NO_x) are the source of aerosol nitrate and participate in nonlinear photochemistry that results in tropospheric ozone. Aerosols influence ozone chemistry by serving as sites for heterogeneous and multiphase reactions. For example, *Dentener and Crutzen* [1993] predicted that heterogeneous reactions of NO₃ and N₂O₅ on sulfate aerosol particles can reduce the global tropospheric average O₃ burden by about 9%. *Zhang et al.* [1994] predicted that interactions of N₂O₅, O₃, and HO₂ radicals with dust particles during a dust outbreak may reduce NO_x levels by up to 50%. Heterogeneous reactions influence the atmospheric cycle of some aerosols. Uptake of HNO₃ and SO₂ by mineral dust may be important in influencing burdens of sulfate and nitrate [*Dentener et al.*, 1996; *Liao et al.*, 2003]. Over the oceans, gas-phase H₂SO₄ and HNO₃ react with sea salt to form sodium sulfate and sodium nitrate, respectively, affecting the partition of NH₃ and HNO₃ between gas and aerosol phases. Sea salt itself is responsible for a fraction of sulfate formation; SO₂ is oxidized by H₂O₂ and O₃ in aerosol water associated with sea salt [*Sievering et al.*, 1991, 1992; *Chameides and Stelson*, 1993; *Erickson et al.*, 1999; *Gurciullo et al.*, 1999], at a rate that depends on sea salt alkalinity.

[4] We examine in this work the radiative forcings of tropospheric ozone and all major aerosol components using the GISS General Circulation Model II' with fully coupled simulations of tropospheric ozone-NO_x-hydrocarbon chemistry and aerosols. The three major components (the GISS GCM, tropospheric chemistry scheme, and aerosol simulation) of this fully coupled model as well as the interactions among these three components are illustrated in Figure 1. Full simulation of tropospheric O₃-NO_x-CO-CH₄-NMHC

chemistry provides consistent chemical fields for aerosol simulation, including SO₂, H₂O₂, and O₃ for in-cloud sulfate formation, SO₂ and OH for gas-phase sulfate formation, HNO₃ and NH₃ for equilibrium partitioning between gas and aerosol phases, as well as reactive hydrocarbons, OH, O₃, and NO₃ for secondary organic aerosol (SOA) formation. We consider uptake of N₂O₅, NO₃, NO₂, and HO₂ by wet aerosols, uptake of HNO₃, SO₂, and O₃ by mineral dust aerosol, as well as uptake of SO₂ by aerosol water associated with sea salt aerosol. Aerosol fields are employed in the calculation of gas-phase photolysis rates.

[5] This study is an extension of the previous global simulation of ozone, sulfate, nitrate, ammonium, black carbon, primary organic carbon, and secondary organic carbon aerosols of *Liao et al.* [2003]. Compared with that work, the major changes are the inclusion of the prediction of global distributions of sea salt and mineral dust and the coupling of heterogeneous reactions on these two classes of particles to the gas-phase chemistry and the cycles of other aerosols.

[6] The goal of this study is to investigate the effects of interactions between gas-phase chemistry and aerosols on current day radiative forcing of ozone and aerosols. We describe the coupled GCM-atmospheric chemistry-aerosol model in section 2. Sections 3 and 4 present simulated global concentrations of sea salt and mineral dust, respectively, with model predictions evaluated by comparisons with measurements. Since simulations of O₃-NO_x-CO-CH₄-NMHC chemistry, SO₄²⁻/NO₃⁻/NH₄⁺/H₂O, and black carbon/organic carbon aerosols in the same GISS GCM II' have been evaluated extensively by *Mickley et al.* [1999], *Adams et al.* [1999], and *Chung and Seinfeld* [2002], respectively, and the current predictions for the most part agree closely with the predictions in those studies, we do not repeat comparisons with measurements for ozone, SO₄²⁻/NO₃⁻/NH₄⁺/H₂O, and carbonaceous aerosols in this work. Section 5 examines the effects of heterogeneous reactions associated with sea salt

Table 1. GCM Chemical Tracers

| Tracers | Composition |
|--|--|
| O _x | O ₃ + O + NO ₂ + 2 × NO ₃ |
| NO _x | NO + NO ₂ + NO ₃ + HNO ₂ |
| HNO ₃ | |
| HNO ₄ | |
| N ₂ O ₅ | |
| PAN | peroxyacetyl nitrate |
| H ₂ O ₂ | |
| CO | |
| C ₃ H ₈ | |
| C ₂ H ₆ | |
| ALK4 | lumped ≥ C ₄ alkanes |
| PRPE | lumped ≥ C ₃ alkenes |
| isoprene | |
| acetone | |
| CH ₃ OOH | |
| CH ₂ O | |
| CH ₃ CHO | |
| RCHO | lumped ≥ C ₃ aldehydes |
| MEK | lumped ≥ C ₄ ketones |
| methy vinyl ketone | |
| methacrolein | |
| MPAN | peroxymethacryloyl nitrate |
| PPN | lumped peroxyacyl nitrates |
| R4N2 | lumped alkyl nitrates |
| SO ₂ | |
| SO ₄ ²⁻ | |
| DMS | |
| NH ₃ | |
| NH ₄ ⁺ | |
| NO ₃ ⁻ | |
| hydrophobic BC | |
| hydrophilic BC | |
| hydrophobic POA | |
| hydrophilic POA | |
| hydrocarbon I | α-pinene, β-pinene, sabinene, Δ ³ -carene, terpenoid ketones |
| hydrocarbon II | limonene |
| hydrocarbon III | α-terpinene, γ-terpinene, terpinolene |
| hydrocarbon IV | myrcene, terpenoid alcohols, ocimene |
| hydrocarbon V | sesquiterpenes |
| 14 gas-phase products | from reactions of hydrocarbon classes I to V with OH, O ₃ , NO ₃ |
| 14 aerosol-phase products | from gas-aerosol partitioning of 14 gas-phase products |
| 11 sea salt tracers | one for each size bin |
| SO ₄ ²⁻ (sea salt) | from sea salt uptake of SO ₂ |
| 6 dust tracers | one for each size bin |
| SO ₄ ²⁻ (dust) | from mineral dust uptake of SO ₂ |
| NO ₃ ⁻ (dust) | from mineral dust uptake of HNO ₃ |
| AlkCa | Ca ²⁺ that is not neutralized by SO ₄ ²⁻ (dust) and NO ₃ ⁻ (dust) |

and mineral dust on concentrations of climate-sensitive species such as sulfate and nitrate. Direct radiative forcing by aerosols and ozone is evaluated in section 6. In section 7, radiative forcing is calculated with all chemistry-aerosol interactions removed to investigate the effect of chemistry-aerosol coupling on radiative forcing.

2. Model Description

2.1. GISS GCM II'

[7] In this study, gas-phase chemistry and aerosols are simulated on-line within the GISS GCM II' [Hansen *et al.*, 1983; Rind and Lerner, 1996; Rind *et al.*, 1999]. The GCM has a resolution of 4° latitude by 5° longitude, with 9 vertical layers centered at 959, 894, 786, 634, 468, 321, 201, 103, and 26.5 mbar. It uses a quadratic upstream scheme for advection of heat, moisture, and tracers. The GCM distinguishes between large scale and convective

clouds. It carries liquid water as a prognostic variable in the large-scale cloud scheme [Del Genio *et al.*, 1996], and moist convection is implemented by a variable mass flux scheme [Del Genio and Yao, 1993]. This version of the GCM uses monthly mean ocean temperature maps. The dynamic time step of the GCM is 1 hour.

2.2. Chemistry Scheme

[8] The gas-phase tropospheric O₃-NO_x-hydrocarbon chemical mechanism and chemical reactions used for the simulations of sulfate, nitrate, ammonium, black carbon, primary organic carbon, and secondary organic carbon aerosols are given in Liao *et al.* [2003]. The suite of tracers transported in the GISS GCM II' is listed in Table 1. We use 24 tracers in the model to describe O₃-NO_x-hydrocarbon chemistry, including odd oxygen (O_x = O₃ + O + NO₂ + 2NO₃), NO_x (NO + NO₂ + NO₃ + HNO₂), N₂O₅, HNO₃, HNO₄, peroxyacetyl nitrate, H₂O₂, CO, C₃H₈, C₂H₆,

($\geq C_4$) alkanes, ($\geq C_3$) alkenes, isoprene, acetone, CH_2O , CH_3CHO , CH_3OOH , ($\geq C_3$) aldehydes, ($\geq C_4$) ketones, methyl vinyl ketone, methacrolein, peroxyacetyl nitrate, lumped peroxyacyl nitrates, and lumped alkyl nitrates. Transporting O_x and NO_x as chemical families reduces the need for tracking many rapidly interchanging gases. Spatially and seasonally varying flux boundary conditions are specified at 150 mbar to represent the cross-tropopause transport of O_3 and reactive nitrogen NO_y [Mickley *et al.*, 1999]. Stratosphere ozone is prescribed by climatology derived from satellite data. Sulfate/nitrate/ammonium/sea salt/water is treated as an internal mixture, which is represented by the aerosol thermodynamics module, ISORROPIA. Black carbon, primary organic carbon/secondary organic carbon, and mineral dust are treated as externally mixed with sulfate/nitrate/ammonium/sea salt/water. Twenty-one tracers are used for the simulations of sea salt and mineral dust aerosols: eleven tracers for eleven size bins of sea salt, one tracer for the uptake of SO_2 by sea salt, six tracers for six size bins of mineral dust, two tracers for dust-associated sulfate and nitrate resulting from dust uptake of SO_2 and HNO_3 , respectively, and one tracer for dust alkalinity. The chemistry scheme includes 225 chemical species and 346 reactions. The chemical mechanism is integrated over 4-hour time steps with a fast Gear solver [Jacobson and Turco, 1994]. Rates of 40 photolysis reactions are computed using the Fast-J code of Wild *et al.* [2000], which accounts for absorption by O_2 and O_3 , Rayleigh scattering, and Mie scattering by clouds and aerosols, using seven wavelength channels of varying widths covering the spectral range from 289 to 800 nm. Although the effects of aerosols on photolysis rates were found to be small when considering predicted monthly mean concentrations of HNO_3 and O_3 [Liao *et al.*, 2003], we account for effects of all aerosols on photolysis rates in this study.

2.3. Sea Salt Cycle

[9] Sea salt aerosol results from the evaporation of sea spray produced by bursting bubbles or wind-induced wave breaking over the oceans. Observations have shown that the radius of sea salt aerosol can range from 0.02 to 60 μm [Fitzgerald, 1991]. To account for the effects of sea salt on radiative forcing and heterogeneous reactions, we use 11 size bins (0.031–0.063, 0.063–0.13, 0.13–0.25, 0.25–0.5, 0.5–1, 1–2, 2–4, 4–8, 8–16, 16–32, 32–64 μm dry radius) following the study of Guelle *et al.* [2001]. Although particles whose radii are larger than 10 μm are not efficient in light scattering, they are important for heterogeneous reactions.

[10] With limited observations available, estimates of sea salt emissions have to rely on empirical generation functions obtained based on measurements. Sea salt emissions depend on surface wind speed over the oceans. Three different formulations were reported in the studies of Monahan *et al.* [1986], Smith and Harrison [1998], and Andreas [1998]. Guelle *et al.* [2001] compared simulated sea salt concentrations and size distributions based on these three generation functions with measurements and found that sea salt particles with dry radius below 4 μm are well represented by Monahan *et al.*'s formulation, while Smith and Harrison's formulation is most appropriate for particles

larger than 4 μm . We use these suggested formulations for the production of sea salt in this study.

[11] We use 11 tracers to treat sea salt mass in each size bin as a tracer; thus, each size bin is represented by one mass continuity equation. The major processes that determine the changes in sea salt mass are transport, emission, dry deposition and wet deposition. We do not consider intersectional mass transfer from coagulation or breaking of the existing particles.

[12] Dry deposition of all GCM tracers is represented by the resistance-in-series scheme of Wesely [1989]. The size-dependent dry deposition velocity of sea salt is computed as shown by Grini *et al.* [2002]. Sea salt aerosol hygroscopicity is calculated by the empirical expression of Gerber [1985],

$$R_w = \left[\frac{C_1 R_d^2}{C_3 R_d^4 - \log S} + R_d^3 \right]^{1/3}, \quad (1)$$

where R_w and R_d are the wet and dry particle radii (in cm), S is the relative humidity expressed as a fraction, and C_1 , C_2 , C_3 , and C_4 are constants whose values are 0.7674, 3.079, 2.573×10^{-11} , and -1.424 , respectively. The density of dry sea salt particles is assumed to be 2.25 g cm^{-3} [Takemura *et al.*, 2000].

[13] Wet deposition is coupled with the GCM treatment of clouds and precipitation. Within clouds, sea salt particles are completely scavenged, and the washout below clouds uses a first-order parameterization that depends on the amount of precipitation [Koch *et al.*, 1999]. Below-cloud scavenging coefficients follow those given in Dana and Hales [1976] and are size-dependent.

2.4. Mineral Dust Cycle

[14] Dust emission is calculated as a function of surface vegetation cover, surface wind speed, and soil moisture. The fractional vegetation cover within each grid box is derived from the $0.5^\circ \times 0.5^\circ$ resolution global surface-type map of Olson [1992] that distinguishes among 56 ecosystems. The emission mass flux of soil dust, F_{dust} in $\text{kg m}^{-2} \text{ s}^{-1}$, is given by the empirical formulation [Gillette, 1978]

$$F_{\text{dust}} = C(u - u_t)^2, \quad (2)$$

where u is the surface wind velocity in m s^{-1} and is predicted by the GCM. u_t is the threshold velocity and is set to be 6.5 m s^{-1} according to Kalma *et al.* [1988]. There are no dust emissions when $u < u_t$. The emission coefficient C of $1.5 \times 10^{-9} \text{ kg s}^2 \text{ m}^{-5}$ is used. We use predicted precipitation to identify if soil is dry and dust emission is possible. We assume dust emissions can occur from a grid only when precipitation over the past 4 hours is less than 1 mm.

[15] Six size bins (0.0316–0.1, 0.1–0.316, 0.316–1.0, 1.0–3.16, 3.16–10, and 10–31.6 μm dry radius) are used to represent mineral dust [Woodward, 2001]. The GCM transports these six size classes of dust as independent tracers. Dust emissions calculated from equation (2) are distributed into each size bin by using the soil-particle size distribution given by Woodward [2001], which was derived from the soil data set of Wilson and Henderson-Sellers [1985].

Table 2. Uptake Coefficients for Heterogeneous Reactions on Aerosol Surfaces

| Species | On Medium | Uptake Coefficients | References |
|-------------------------------|---------------------------|---|-----------------------------------|
| N ₂ O ₅ | wet aerosols ^a | 0.1 | <i>Jacob [2000]</i> |
| NO ₃ | wet aerosols | 0.001 | <i>Jacob [2000]</i> |
| NO ₂ | wet aerosols | 0.0001 | <i>Jacob [2000]</i> |
| HO ₂ | wet aerosols | 0.2 | <i>Jacob [2000]</i> |
| SO ₂ | mineral dust | 3 × 10 ⁻⁴ (RH < 50%) 0.1 (RH > 50%) | <i>Dentener et al. [1996]</i> |
| HNO ₃ | mineral dust | 0.1 | <i>Dentener et al. [1996]</i> |
| O ₃ | mineral dust | 5 × 10 ⁻⁵ | <i>Dentener et al. [1996]</i> |
| SO ₂ | sea salt | 0.05 (RH > 50%) 0.005 (RH < 50%) | <i>Song and Carmichael [2001]</i> |

^aSO₄²⁻/NO₃⁻/NH₄⁺/NaCl/H₂O, OC, sea salt, and mineral dust are considered to be wet aerosols when RH > 50%.

[16] Dry deposition of mineral dust follows the scheme for sea salt. Although mineral dust may absorb water at high relative humidity, we use dry size in the calculation of dry deposition since the extent of water uptake by dust is not established. Wet deposition of dust aerosol includes in-cloud and below-cloud scavenging. For in-cloud scavenging of dust particles, different assumptions have been made in previous studies. *Tegen et al. [2002]* assumed that dust is nonhygroscopic and does not form cloud condensation nuclei. *Ginoux et al. [2001]* assumed that the in-cloud scavenging parameters for dust are the same as those for sulfate, whereas *Zender et al. [2003]* used a scavenging coefficient of 0.1 for dust nucleation scavenging to account for the hydrophobic nature of mineral aerosol. In this study, we follow the assumption of *Zender et al. [2003]* for the scavenging of dust particles within both convective and large-scale clouds. Below-cloud scavenging of dust employs the same scheme used for sea salt aerosol.

2.5. Aerosol Equilibrium

[17] Volatile atmospheric species tend to partition themselves between gas and aerosol phases in accordance with thermodynamic equilibrium [*Seinfeld and Pandis, 1998*]. As in *Liao et al. [2003]*, the thermodynamic equilibrium model ISORROPIA [*Nenes et al., 1998*] is employed to simulate the partitioning of inorganic volatile species. The presence of sea salt aerosol influences the partitioning of NH₃, HNO₃, HCl, and water, because sodium and chloride react with other aerosol components to form a series of compounds, such as ammonium chloride, sodium nitrate, sodium sulfate, and sodium bisulfate, in the sodium-ammonium-chloride-sulfate-nitrate-water aerosol system. At RH < 100%, ISORROPIA computes the equilibrium composition of an internally mixed aerosol consisting of sulfate, nitrate, chloride, ammonium, sodium, and water. The inputs needed by ISORROPIA are the total concentrations of NH₃ + NH₄⁺, HNO₃ + NO₃⁻, SO₄²⁻, HCl + Cl⁻, and Na⁺, together with the ambient relative humidity and temperature.

2.6. Heterogeneous Reactions

[18] Hydrolysis of N₂O₅ on wetted aerosol surfaces of sulfate, nitrate, ammonium, organic carbon, and sea salt is considered in this study. We assume this reaction also occurs on mineral dust aerosol when ambient relative humidity exceeds 50%, because, as can be seen later in this section, the uptake coefficient for dust uptake of SO₂ is

assumed to be much larger when relative humidity exceeds 50% than when it is lower than 50%, and therefore we assume dust particles are more hygroscopic when RH ≥ 50%. The HNO₃ produced equilibrates between the gas and aerosol phases. The irreversible absorption of NO₃, NO₂, and HO₂ is accounted for on the same wetted aerosol surfaces where hydrolysis of N₂O₅ occurs. The uptake coefficients used to calculate the first-order loss rate of these species on aerosol surfaces are summarized in Table 2.

[19] We treat the fraction of SO₂ that is scavenged by sea salt and oxidized by O₃ and H₂O₂ in water associated with sea salt as a tracer. When SO₂ is transported to the surface of sea salt particles, some fraction is scavenged by these particles. The scavenged SO₂ is absorbed into the aqueous phase as determined by its Henry's law constant, and then oxidized by H₂O₂ and O₃ to form non-sea-salt sulfate. The change in SO₂ concentration, [SO₂], by scavenging and oxidation loss in sea salt particles is calculated by

$$\frac{d[\text{SO}_2]}{dt} = -k_{\text{tot}}[\text{SO}_2] \quad (3)$$

and k_{tot} is given by [*Brasseur et al., 1999; Mari et al., 1999*]

$$\frac{1}{k_{\text{tot}}} = \frac{1}{k_t} + \frac{1}{(k_{\text{O}_3} + k_{\text{H}_2\text{O}_2})}, \quad (4)$$

where $k_{\text{H}_2\text{O}_2}$ and k_{O_3} are first-order aqueous phase oxidation rate constants of SO₂ by H₂O₂ and O₃, respectively, and are calculated by using the same aqueous reaction rates and dissociation rates as those used for in-cloud sulfate formation [*Liao et al., 2003*]. The water content of each particle is calculated from the difference between its dry and wet volume. k_t is the first-order gas-to-particle transfer rate and is represented by [*Schwartz, 1986*]

$$k_t = \sum_i A_i \left(\frac{R_{wi}}{D_g} + \frac{4}{v\gamma} \right)^{-1}, \quad (5)$$

where $A_i = 4\pi R_{wi}^2 N_i$ is the total surface area (cm² cm⁻³) of sea salt particles in size bin i , N_i (particles cm⁻³) is the number concentration of sea salt in that size bin, R_{wi} (cm) is the arithmetic mean of the wet radius determined by equation (1), D_g (cm² s⁻¹) is the gas-phase molecular diffusion coefficient of SO₂ in air, v is the mean molecular speed (cm s⁻¹), and γ is the uptake coefficient. On sea salt particles, $\gamma(\text{SO}_2)$ is assumed to be 0.05 for RH > 50% and 0.005 when RH < 50% [*Song and Carmichael, 2001*].

[20] The oxidation of SO₂ by O₃ is sensitive to pH value of the sea salt particles. *Sievering et al. [1992]* and *Chameides and Stelson [1993]* reported that sea salt pH ranges from 6.5 to 7.5, so we assume here that sea salt particles have a constant pH of 7.0. Although sea salt alkalinity is expected to be titrated and fall as sulfuric acid continues to be generated by the reaction between dissolved S(IV) and O₃, recent laboratory studies show that sodium hydroxide is generated upon reaction of deliquesced sodium chloride particles with gas-phase hydroxide, which may lead to the increase in sea salt alkalinity and maintains the uptake and oxidation of sulfur dioxide to sulfate in sea-salt particles [*Laskin et al., 2003*]. Assuming a pH of 7.0 implies that sea

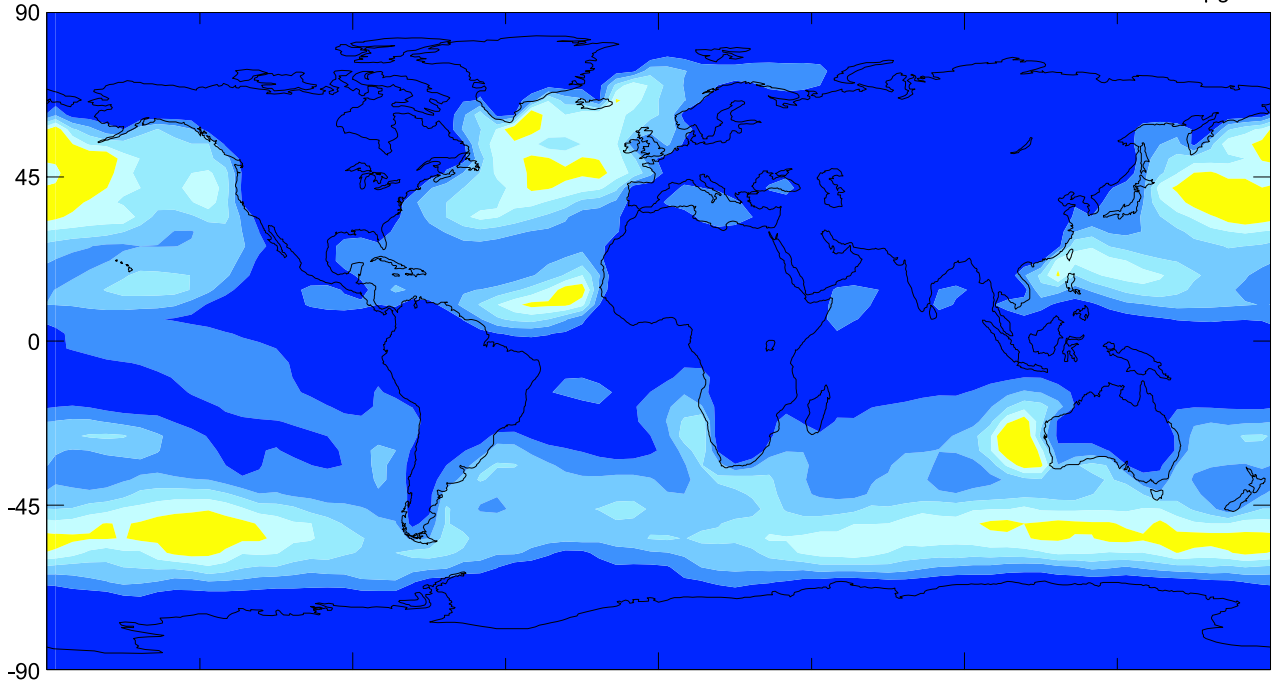
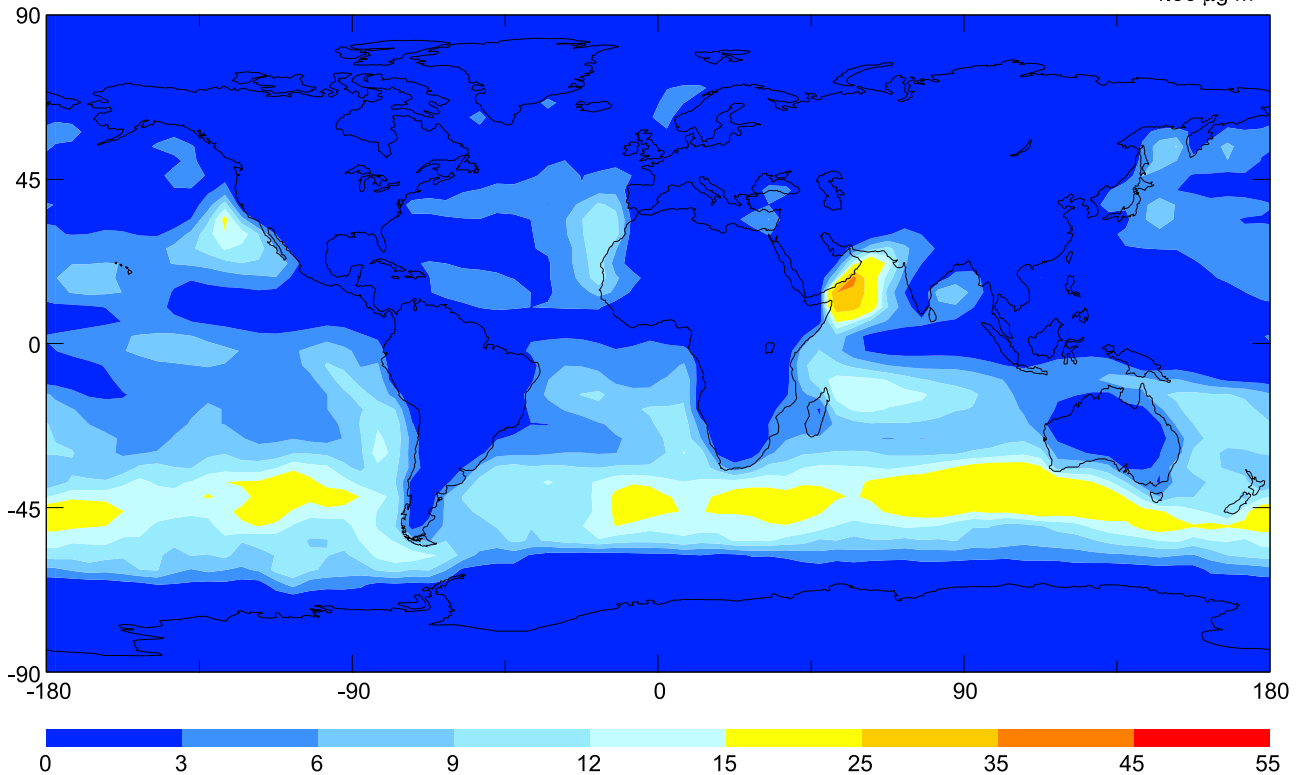
4.46 $\mu\text{g m}^{-3}$ 4.56 $\mu\text{g m}^{-3}$ 

Figure 2. Predicted monthly mean sea salt concentrations ($\mu\text{g m}^{-3}$) at the GCM surface layer for (top) January and (bottom) July. Above each panel the global mean concentration is indicated.

salt particles have sufficient buffering capacity and the sea salt uptake of SO_2 calculated in this work may represent an upper limit.

[21] Studies have shown that mineral dust aerosol can take up SO_2 , HNO_3 , and O_3 and influence chemistry of gas-

phase species and aerosols [Dentener *et al.*, 1996; Galy-Lacaux and Modi, 1998; Tabazadeh *et al.*, 1998; Song and Carmichael, 2001; Galy-Lacaux *et al.*, 2001; Bauer *et al.*, 2004]. For the uptake of SO_2 , HNO_3 and O_3 by mineral dust, we use an uptake coefficient $\gamma(\text{HNO}_3)$ of 0.1, $\gamma(\text{SO}_2)$

of 3×10^{-4} for regions with $RH < 50\%$, $\gamma(\text{SO}_2)$ of 0.1 when $RH > 50\%$, and $\gamma(\text{O}_3)$ of 5×10^{-5} [Dentener et al., 1996]. It should be noted that heterogeneous reactions on dust particles are highly uncertain as dust uptake may be influenced by temperature, relative humidity, and mass of dust. For example, dry dust $\gamma(\text{HNO}_3)$ determined by Fenter et al. [1995] and Hanisch and Crowley [2001] is about one to two orders of magnitude greater than that determined by Goodman et al. [2000] and Underwood et al. [2001], and the uptake of HNO_3 increases by nearly a factor of 50 when RH increases from near 0 to 16%. In the present modeling study we use $\gamma(\text{HNO}_3)$ of 0.1 based on the uptake coefficients observed by Hanisch and Crowley [2001] and the modeling work of Bauer et al. [2004], who used $\gamma(\text{HNO}_3)$ of 0.1 to simulate uptake of HNO_3 by mineral dust and found close agreement between predicted and measured concentrations of HNO_3 throughout the dust events observed during the MINATROC field campaign. $\gamma(\text{HNO}_3)$ of 0.1 on dust particles represents an upper limit to the HNO_3 uptake coefficients (V. H. Grassian, personal communication, 2003), which should be kept in mind when evaluating model results.

[22] SO_2 and HNO_3 deposited on dust particles are assumed to exist in the forms of SO_4^{2-} and NO_3^- , respectively. Following the study of Dentener et al. [1996], we assume that uptake of SO_2 and HNO_3 by mineral dust takes place only when the dust alkalinity exceeds the acidity from the dust-associated sulfate and nitrate. If alkalinity is contributed by the calcium ion, uptake of SO_2 and HNO_3 occurs when $[\text{Ca}^{2+}] - [\text{SO}_4^{2-}(\text{dust})] - 0.5[\text{NO}_3^-(\text{dust})] > 0$. We assume that the Ca^{2+} content of freshly emitted dust is 5% by weight [Dentener et al., 1996]. The direct GCM simulation of the dust cycle provides a consistent treatment of nitrate and sulfate associated with dust, and makes it possible to compute dust alkalinity. Dust-associated sulfate and nitrate are treated as tracers. In each grid cell, we calculate the formation of sulfate (or nitrate) on dust particles in each size bin and then sum over all the six size bins to get the total amount. For dry deposition of dust-associated sulfate (or nitrate), we use an average dry deposition velocity that is averaged over the six size bins and weighted by the dust mass in each size bin, since we calculate size-dependent dry deposition velocity for dust particles. Similarly, we use an average washout rate to calculate the removal of dust-associated sulfate (or nitrate) in each grid cell. Dust alkalinity is simulated by treating the mass of Ca^{2+} that is not neutralized by SO_4^{2-} and NO_3^- (hereinafter referred to as *AlkCa*) as a tracer. In each grid, the mass of *AlkCa* has to be greater than zero for dust particles to take up SO_2 and HNO_3 . The dry and wet deposition of *AlkCa* follow the treatment for the deposition of dust-associated sulfate and nitrate.

3. Simulation of Sea Salt Aerosol

[23] The base simulation was performed with coupled atmospheric dynamics, gas-phase chemistry, as well as sulfate, nitrate, ammonium, black carbon, organic carbon, sea salt and mineral dust aerosols for present-day conditions. The simulation was conducted for an 18-month period, with the first 6 months ignored for spin-up. The

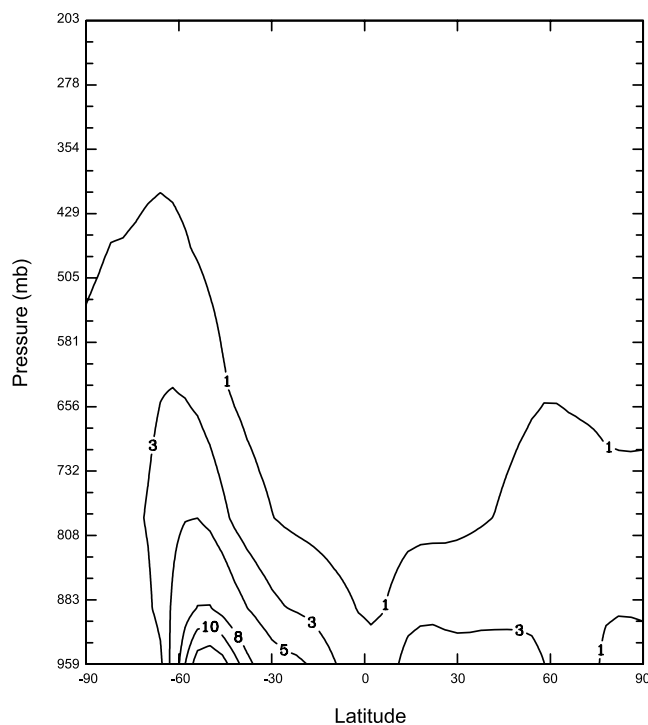


Figure 3. Predicted annual, zonal average sea salt concentrations ($\mu\text{g m}^{-3}$).

results presented in this paper are from this one-year simulation, except where noted. The emission inventories for the simulations of gas-phase chemistry, sulfate, nitrate, ammonium, black carbon, organic carbon are those given in Liao et al. [2003].

[24] Based on the wind velocities predicted by the GISS GCM II', the estimated sea salt emission flux is 6056 Tg yr^{-1} in this study. This value is in close agreement with the estimates of 5900 Tg yr^{-1} obtained by Tegen et al. [1997] for the particles in the size range $2\text{--}16 \mu\text{m}$ and 6500 Tg yr^{-1} reported by Grini et al. [2002] for the particles in $0.03\text{--}25 \mu\text{m}$ range.

3.1. Predicted Concentrations of Sea Salt

[25] The predicted distributions of sea salt concentrations in the lowest model layer are shown in Figure 2 for January and July. High NaCl concentrations, 15 to $25 \mu\text{g m}^{-3}$, are found over midlatitudes in Northern Hemisphere in winter and in Southern Hemisphere in both winter and summer, corresponding to the strong winds in these areas. Both the magnitudes and distributions predicted here are in good agreement with those of Grini et al. [2002]. Sea salt concentrations decrease rapidly with height, which can be seen from the predicted zonal annual average sea salt concentrations (Figure 3). Zonal annual-average concentrations exceeding $3 \mu\text{g m}^{-3}$ can only be found below 600 mbar altitude. Highest surface concentrations are found in the midlatitudes in the Southern Hemisphere, which was also predicted by Grini et al. [2002].

[26] The predicted global and annual mean burden of sea salt is 13.6 mg m^{-2} , which is close to the predicted values of 12 mg m^{-2} by Grini et al. [2002] and 11 mg m^{-2} by Takemura et al. [2000]. Sea salt lifetime calculated in this

Table 3. Measurements Selected for Comparison With GCM Predictions of Sea Salt Aerosol

| Site | Latitude | Longitude | Time Period | Reference |
|---------------------------|----------|-----------|------------------------|------------------------------------|
| Alert, Canada | 82.4°N | 62.3°W | 13 years average | <i>Gong et al.</i> [1997] |
| Heimaey, Iceland | 63.3°N | 20.2°W | July 1991 to Aug. 1994 | <i>Gong et al.</i> [1997] |
| Mace Head, Ireland | 53.3°N | 9.9°W | Aug. 1988 to July 1993 | <i>Gong et al.</i> [1997] |
| Bermuda, UK | 32.3°N | 64.9°W | 1982–1994 | <i>Gong et al.</i> [1997] |
| Miami, USA | 25.8°N | 80.3°W | 1989–1998 | D. Savoie (personal communication) |
| Midway, USA | 28.2°N | 177.4°W | 1982–1994 | <i>Tegen et al.</i> [1997] |
| Cape Grim, Australia | 40.7°S | 144.7°E | Dec. 1988 to May 1993 | <i>Gong et al.</i> [1997] |
| Norfolk Island, Australia | 29.1°S | 168.0°E | May 1983 to Feb. 1997 | D. Savoie (personal communication) |
| Yate, New Caledonia | 22.2°S | 167.0°E | Aug. 1983 to Oct. 1985 | D. Savoie (personal communication) |

study is 0.4 day, which is shorter than the 0.8 day calculated by *Takemura et al.* [2000].

3.2. Comparison With Sea Salt Measurements

[27] In this section, predicted seasonal variations of sea salt aerosol concentrations are compared with measurements for a number of coastal and island stations. Validation

of GCM predictions requires long term measurements, but unfortunately such measurements are quite limited for sea salt aerosol. The measurements we use here are listed in Table 3. At each site, monthly mean measurements that are averaged over the observation period (several years) are compared to model predictions from the one-year base simulation (Figure 4). We also present in Figure 4 the

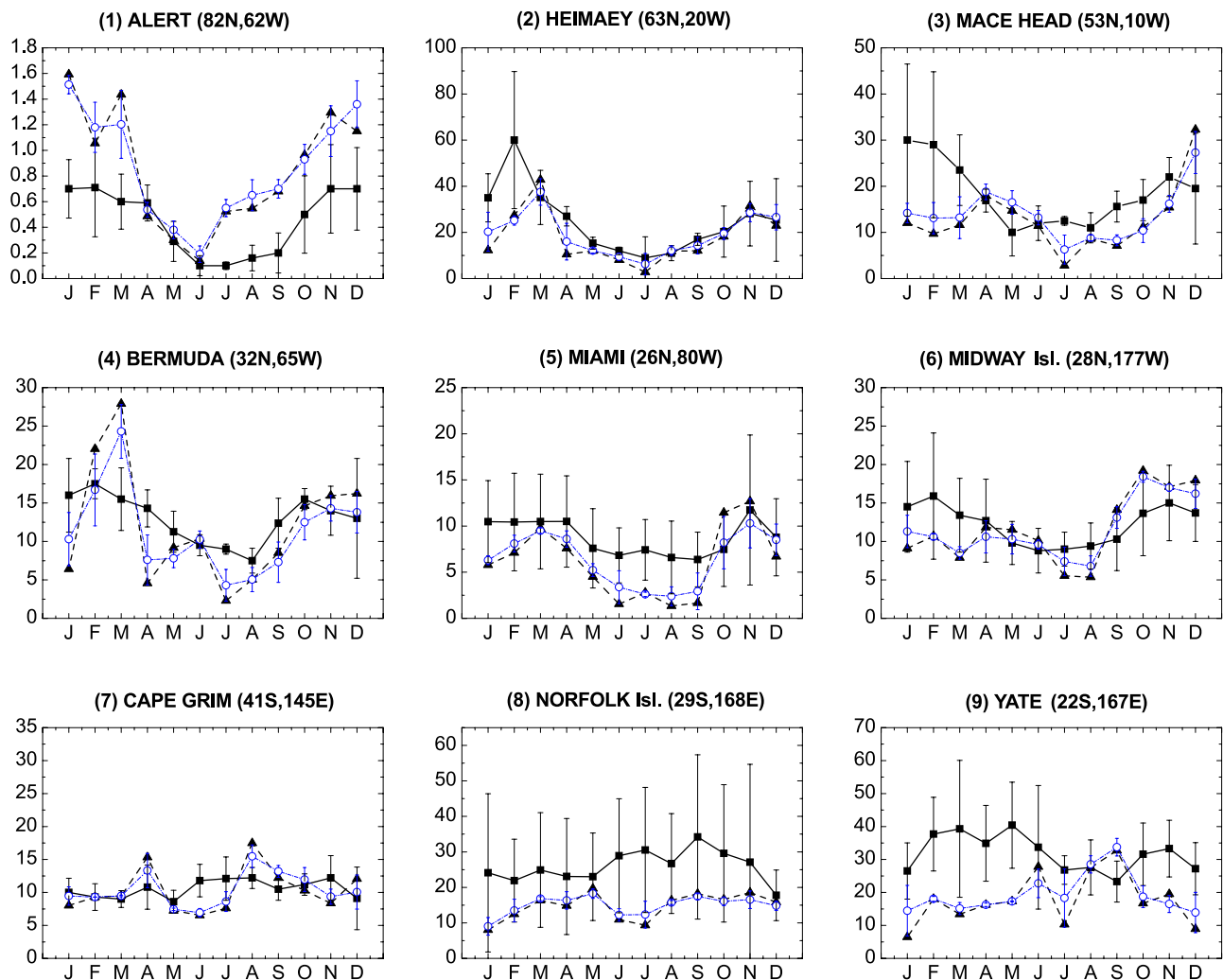


Figure 4. Comparison of predicted surface layer sea salt concentrations ($\mu\text{g m}^{-3}$) with measurements at selected locations. Detailed information about measurements is given in Table 3. Squares represent observations, triangles are GCM predictions for year 1 of the simulation, and circles are the model results for years 1–3 of the simulation. The error bars indicate one standard deviation.

averaged concentrations and standard deviations from a three-year simulation to illustrate the interannual variability. At most sites the model captures the sea salt seasonal variations rather well. Figures 4(1) to 4(3) show the comparisons at three high- to midlatitude sites in the Northern Hemisphere: Alert, Canada (82.4°N, 62.3°W), Heimaey in Iceland (63.3°N, 20.2°W), and Mace Head (53.3°N, 9.9°W) on the west coast of Ireland. At Alert, during the months of April to June, the predictions match the measurements well, but the model overestimates sea salt concentrations in other months by about 100%. Predictions agree closely with measurements at Heimaey in both magnitude and timing. At Mace Head, the model reproduces the observed concentrations fairly well from April to November, but underpredicts concentrations in January–March while overpredicting in December; the base simulation underestimates sea salt concentration by 66% in February and overestimates by 64% in December.

[28] Figures 4(4) to 4(6) compare predictions at three sites in the subtropical regions in the Northern Hemisphere. Both observation and prediction show minimum concentrations during June–August at Bermuda (32.3°N, 64.9°W) (Figure 4(4)), but predictions show larger variation in magnitude than measurements. The model underestimates sea salt concentration in July by 72% in the base simulation and by 52% in the three-year simulation.

[29] At Miami (25.8°N, 80.3°W) (Figure 4(5)), the model tends to underpredict sea salt concentrations; the simulated concentrations are about 75% lower than the observations in Northern Hemisphere summer. The model captures the seasonal variation at Midway Island (28.2°N, 177.4°W) (Figure 4(6)); concentrations exhibit a minimum from June to August.

[30] Comparisons for three sites in the Southern Hemisphere are shown in Figures 4(7) to 4(9). At Cape Grim (40.7°S, 144.7°E) and Norfolk Island (29.1°S, 168°E), both the measurements and predictions do not show strong seasonal variations. The model underestimates the concentrations throughout the year at Norfolk Island; the annual mean value of predicted concentrations from the base simulation is 43% lower than that of measurements. Concentrations at Yate (22.2°S, 167.0°E), New Caledonia, are also underpredicted in most of the months, possibly caused by the representation of surface winds by the GCM in this area.

[31] To evaluate the overall performance in predicting sea salt mass concentrations, we compare predicted monthly mean concentrations from the base simulation with observations in a scatterplot (Figure 5). Most model results agree with the observations within a factor of two for mass concentrations. The mean bias, normalized mean bias, mean error, and normalized mean error for the predicted sea salt concentrations are $-4.48 \mu\text{g m}^{-3}$, -27.9% , $6.7 \mu\text{g m}^{-3}$ and 41.6% , respectively. Negative mean bias indicates that the model has a tendency to underestimate sea salt mass concentrations. Underestimations occur at all latitudes, as shown by the data points classified according to the latitude.

4. Simulation of Mineral Dust Aerosol

4.1. Global Distributions of Dust

[32] The range of magnitudes of global dust emissions estimated in previous studies is large, varying from 128 to

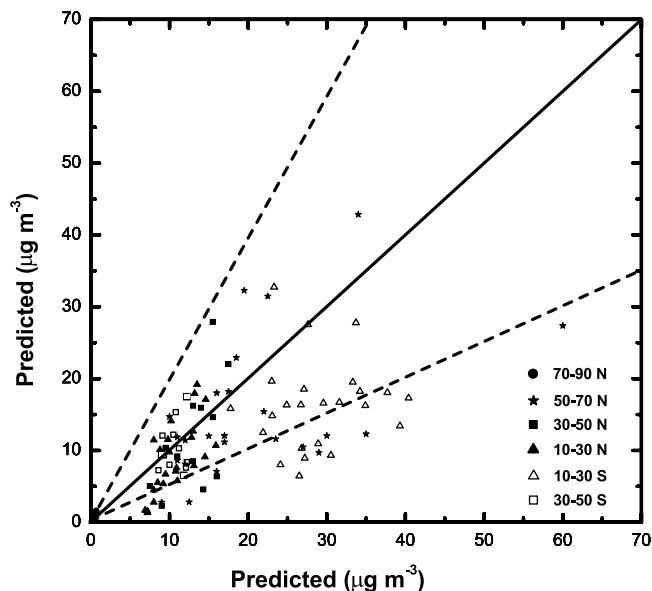


Figure 5. Predicted monthly mean sea salt concentrations from year 1 simulation versus observations for all the locations given in Table 3. Data points are classified by latitudes. Solid line indicates 1:1 ratio, and dashed lines indicate 2:1 and 1:2 ratios.

5000 Tg yr^{-1} [Pye, 1987]. The calculated global dust emission in the present work is 1784 Tg yr^{-1} , in which 1481 Tg yr^{-1} is for particles with radius less than $10 \mu\text{m}$. These emission estimates are in close agreement with the total emission of $1604\text{--}1956 \text{ Tg yr}^{-1}$ predicted by Ginoux *et al.* [2001], the emission of 1250 Tg yr^{-1} for particles with radius less than $8 \mu\text{m}$ reported by Tegen and Fung [1995], and the range of $1312 \pm 97 \text{ Tg yr}^{-1}$ simulated by Perlwitz *et al.* [2001].

[33] Seasonal averaged global dust distributions are shown in Figure 6. The source regions appear clearly in this figure as well as the patterns resulting from long-range transport. Concentrations exceeding $250 \mu\text{g m}^{-3}$ are found over North Africa throughout the year and over Central and Eastern Asia in March–April–May. Dust concentrations over the Sahara, Central and Eastern Asia, and US are highest in Northern Hemisphere spring, which agree with observations [Sirokko and Sarntheim, 1989; Merrill *et al.*, 1989; Swap *et al.*, 1996; Parungo *et al.*, 1995; Pye, 1987]. Over the Sahara, the area with concentrations higher than $250 \mu\text{g m}^{-3}$ is the smallest in June–July–August, corresponding to the minimum dust emissions in this season [Swap *et al.*, 1996]. The model also captures the two major dust plumes generated from the dust transport. One plume extends from the west coast of North Africa to the North Atlantic Ocean and northeastern coast of South America and the other one covers from eastern China to Korea, Japan, and the North Pacific Ocean. Dust distributions predicted in this study are generally in agreement with those simulated by Ginoux *et al.* [2001], except the maximum dust concentrations over the Arabian Peninsula are predicted to occur in September while these were predicted in June–July–August in the study of Ginoux *et al.* [2001], which may result from the differences between the current

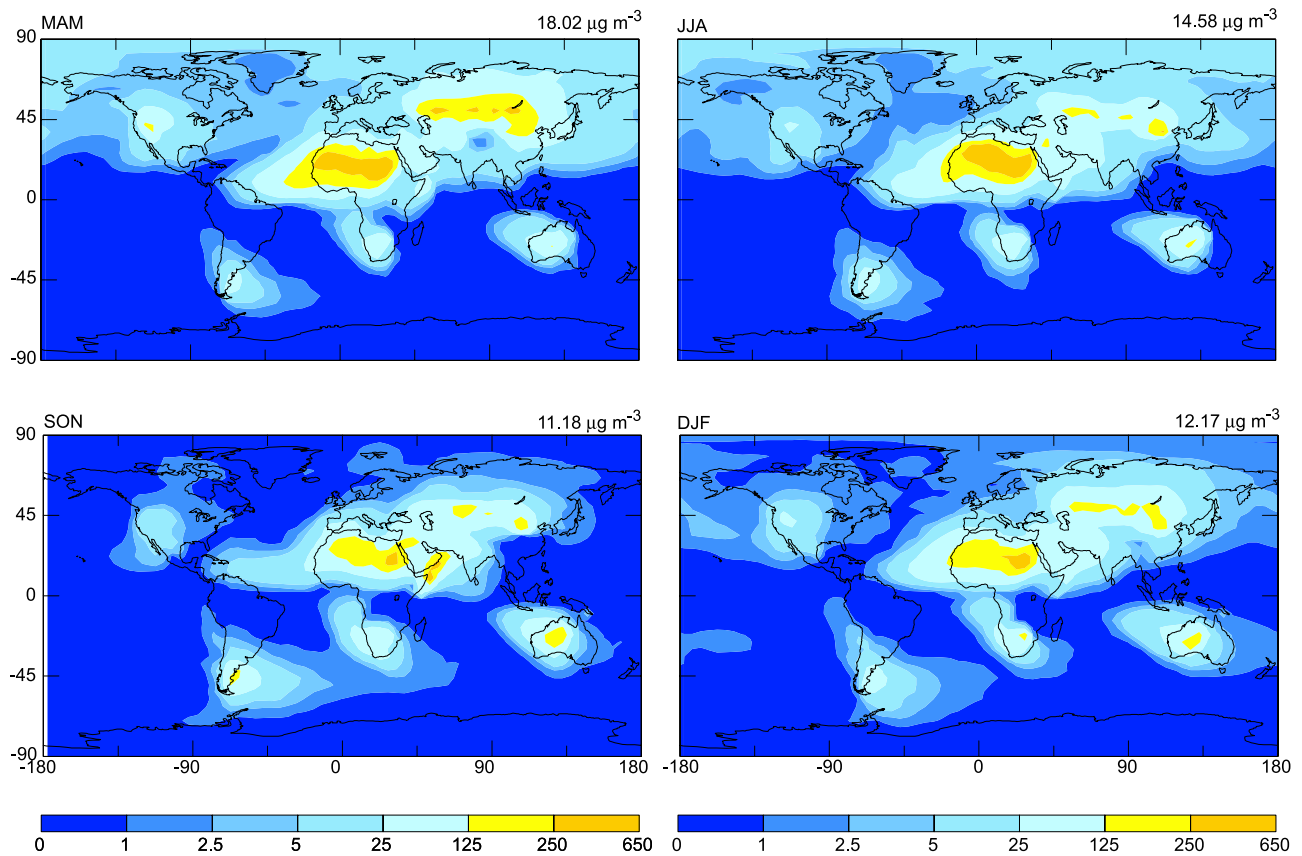


Figure 6. Predicted seasonal averaged mineral dust concentrations ($\mu\text{g m}^{-3}$) at the GCM surface layer for March–April–May (MAM), June–July–August (JJA), September–October–November (SON), and December–January–February (DJF). Above each panel the seasonal and the global mean concentration is indicated.

GCM predicted wind fields and the assimilated fields used by *Ginoux et al.* [2001].

[34] The annual budget for mineral dust aerosol is shown in Table 4 for each size class. The atmospheric burden of dust is predicted to be 18.1 Tg, of which 97% represents particles in the 0.1–10 μm size range. Dry deposition is the major process for dust loss; dust dry deposition is 1490 Tg yr^{-1} and accounts for 87% of the total dust loss. Wet deposition is predicted to be 223 Tg yr^{-1} . The lifetime of the smallest size class is about 4 weeks and that of the largest size class is 0.7 day. The average lifetime estimated for dust particles over the whole size range is 3.9 days.

[35] The calculated burden of 18.1 Tg is within the range of previous model estimates. *Tegen and Lacis* [1996] reported that the dust mass loading is 36.6 mg m^{-2} for particles in the range of 0.1 to 10 μm , which corresponds to a burden of 18.7 Tg. The dust burden was estimated to be 13.8 Tg by *Takemura et al.* [2000] and 31–40 Tg by *Ginoux et al.* [2001] for the 0.1–10 μm size range. The large differences between these studies are a result of large uncertainties in emissions and of the different meteorological fields and schemes used for deposition calculations.

4.2. Comparison of Predicted Dust Concentrations With Observations

[36] Figure 7 shows the comparisons of the predicted monthly dust concentrations from the base simulation with

the observations made at the stations of the University of Miami Aerosol Network [*Prospero, 1996*]. To show the interannual variability in model predictions, the averaged concentrations and standard deviations from a three-year simulation are also presented in Figure 7.

[37] At Izana (28.3°N, 16.5°W) (Figure 7(1)), a site very close to the dust sources in North Africa, the model is able to capture the maximum concentration associated with the maximum dust activities over the Sahara and the Sahel region in Northern Hemisphere spring, but the predicted maximum based on the GCM predicted winds occurs one month later than observed. The magnitude of predicted concentrations at Izana agrees with that of observations throughout the year.

[38] The concentrations at Barbados (13.2°N, 59.4°W), Miami (25.8°N, 80.3°W), Bermuda (32.3°N, 64.9°W),

Table 4. Global Annual Budget for Mineral Dust

| Size Class, μm | Emission, Tg yr^{-1} | Dry Deposition, Tg yr^{-1} | Wet Deposition, Tg yr^{-1} | Burden, Tg | Lifetime, days |
|---------------------------|-------------------------------|-------------------------------------|-------------------------------------|------------|----------------|
| 0.03–0.1 | 5.14 | 1.2 | 3.9 | 0.4 | 28.8 |
| 0.1–0.3 | 19.86 | 10.5 | 9.4 | 0.6 | 11.4 |
| 0.3–1 | 157 | 107.4 | 49.6 | 3.8 | 9.1 |
| 1–3 | 553 | 422.7 | 130.3 | 8.8 | 6.2 |
| 3–10 | 746 | 660.2 | 85.8 | 3.9 | 2.0 |
| 10–32 | 303 | 288.3 | 14.8 | 0.6 | 0.7 |
| 0.03–32 | 1784 | 1490.3 | 293.8 | 18.1 | 3.9 |

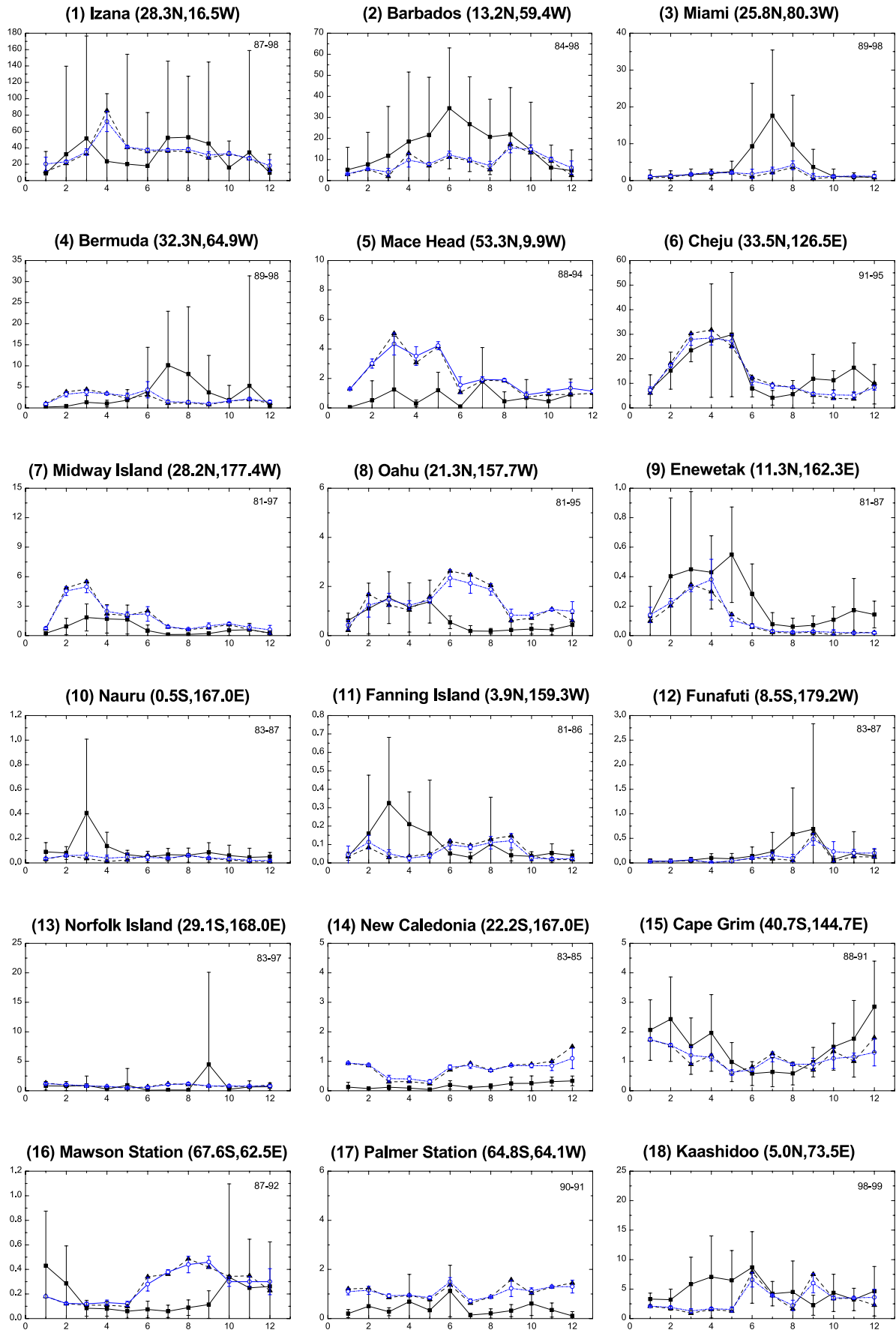


Figure 7

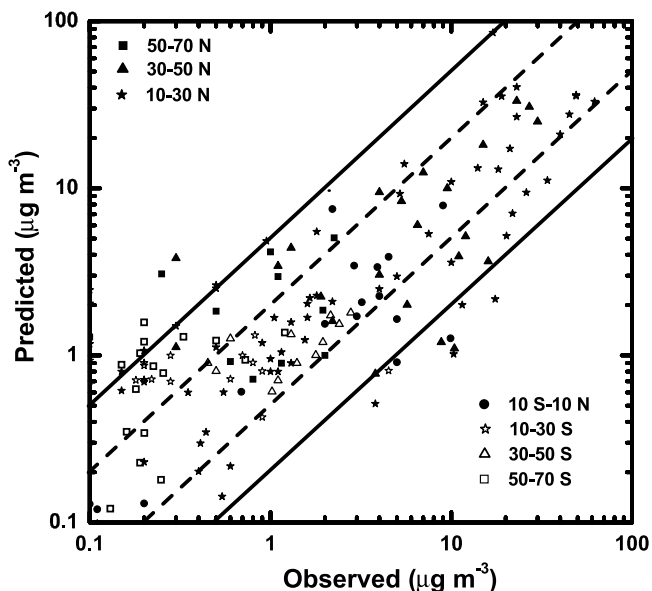


Figure 8. Predicted monthly mean mineral dust concentrations from year 1 simulation versus observations used in Figure 7. Data points are classified by latitudes. Solid lines indicate 5:1 and 1:5 ratios, and dashed lines indicate 2:1 and 1:2 ratios.

and Mace Head (53.3°N, 9.9°W) (Figures 7(2)–7(5)) are mainly influenced by the dust plume transported from North Africa to the Atlantic Ocean. The model tends to underestimate concentrations at Barbados and overestimate at Mace Head. Predicted concentrations at Miami and Bermuda are much lower than the measured values in July and August, implying that the GCM does not generate strong enough winds about the Bermuda High, which is expected to intensify in June–July–August.

[39] Figures 7(6) to 7(8) show the comparisons at three stations, Cheju (33.5°N, 126.5°E), Midway Island (28.2°N, 177.4°W), and Oahu (21.3°N, 157.7°W), located downwind of Asian sources. At these three sites, the model captures the high dust concentrations associated with Asian dust in Northern Hemisphere spring. The peak concentration at Cheju agrees with the observation very well, but the predicted concentrations at Midway Island in February and March and at Oahu in Northern Hemisphere summer are several factors higher than those observed, which may result from the representation of deposition based on the GCM predicted meteorological conditions.

[40] Enewetak (11.3°N, 162.3°E), Nauru (0.5°S, 167.0°E), Fanning Island (3.9°N, 159.3°W), and Funafuti (8.5°S, 179.2°W) (Figures 7(9) to 7(12)) are four sites located over the Pacific Ocean significantly removed from dust sources. At Enewetak, the model predictions match the measured concentrations fairly well. Predicted concentrations have the same behavior at Nauru and Fanning

Island; the predicted concentrations are underestimated by about 90% in March but agree closely with measured concentrations in the rest of the year, possibly because of the representation of the winds by the GCM. At Funafuti, the model predicts concentrations and seasonal variation very well.

[41] Norfolk Island (29.1°S, 168.0°E), New Caledonia (22.2°S, 167.0°E), and Cape Grim (40.7°S, 144.7°E) (Figures 7(13) to 7(15)) are located near the dust sources in Australia. At Norfolk Island, the magnitude of predicted concentrations is close to that of measurements in all months except in September when the measured peak concentration is not captured by the model. At New Caledonia, the measured concentrations are close to zero throughout the year, but the predicted concentrations are about $1 \mu\text{g m}^{-3}$ from June to February. Since the measured concentrations at Norfolk Island, a station 5° south of New Caledonia, are generally in the range of 1 to $4 \mu\text{g m}^{-3}$, the overestimation at New Caledonia suggests that the GCM has predicted an eastward and southeastward transport of Australian dust instead of the measured southeastward transport. At Cape Grim, the model reproduces the concentrations fairly well in both magnitude and seasonal variation.

[42] The model tends to overestimate the concentrations at Mawson station (67.6°S, 62.5°E) and Palmer Station (64.8°S, 64.1°W) (Figures 7(16) and 7(17)), the two stations in Antarctica. The concentrations predicted at Mawson are less than $0.5 \mu\text{g m}^{-3}$, and the predicted concentrations during June–September are about four times higher than the measurements. Levels at Palmer Station are affected by the Patagonia Desert, so we may be overestimating the dust sources from this region.

[43] Kaashidhoo (5.0°N, 73.5°E) is the only site located in the Indian Ocean. The peak concentration in June is related to the strong northeast monsoon winds in this season, which is captured very well.

[44] The overall model performance is shown by the scatterplot (Figure 8) that uses all the measurements in Figure 7. Predicted dust concentrations from the one-year base simulation are generally within a factor of 5 of observations. The mean bias, normalized mean bias, mean error, and normalized mean error for the predicted dust concentrations are $-0.3 \mu\text{g m}^{-3}$, -7.1% , $2.6 \mu\text{g m}^{-3}$, and 61.0%, respectively.

5. Heterogeneous Reactions on Sea Salt and Mineral Dust Particles

5.1. Influence of Sea Salt on Sulfate and Nitrate Concentrations

5.1.1. Sea Salt Uptake of SO_2

[45] The oxidation of SO_2 by H_2O_2 and O_3 in water associated with sea salt aerosol is similar to that occurring in cloud droplets. Ozone plays a dominant role in the oxidation in sea salt particles since sea salt particles

Figure 7. Comparison of predicted surface layer mineral dust concentrations ($\mu\text{g m}^{-3}$) with measurements at University of Miami stations. Squares represent observations, triangles are GCM predictions for year 1 of the simulation, and circles are the model results for years 1–3 of the simulation. The error bars indicate one standard deviation. Site location and the measurement period are indicated for each site.

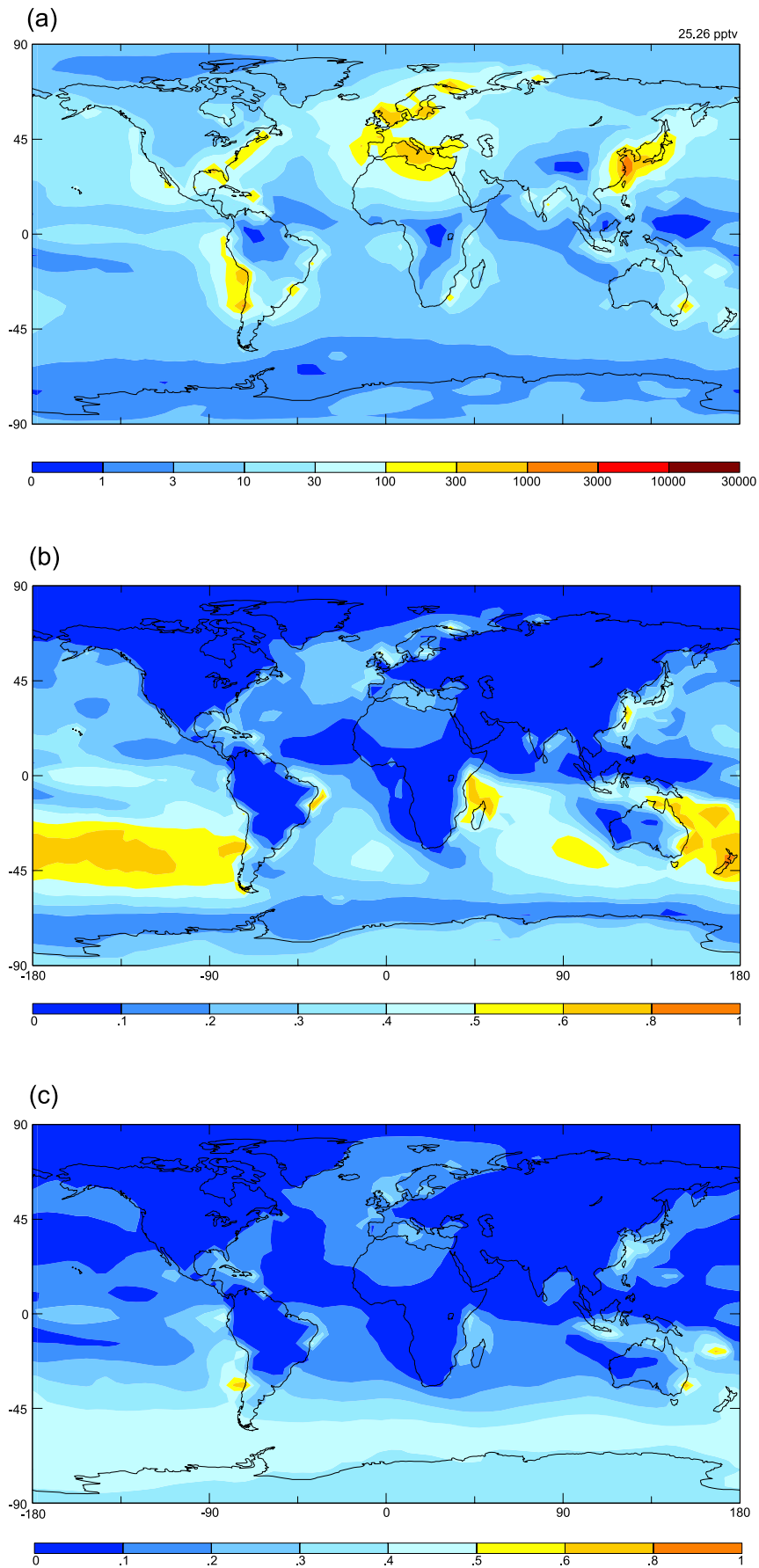


Figure 9

emitted from the oceans usually have high pH values. The fraction of SO_2 that is converted to sulfate on coarse sea salt particles falls out of the atmosphere quickly, leading to the removal of SO_2 from the marine boundary layer [Mari *et al.*, 1999]. The gas-to-particle transfer rates calculated from equation (5) are high where sea salt concentrations are high (see Figure 2), with the highest values reaching $3.4 \times 10^{-3} \text{ s}^{-1}$ over the midlatitudes in the Southern Hemisphere. The magnitude (10^{-3} to 10^{-4} s^{-1}) of these calculated transfer rates is comparable to those calculated by Dentener and Crutzen [1993] for the removal of N_2O_5 on sulfate and sea salt aerosols. The aqueous oxidation rates, dominated by the reaction of SO_2 with O_3 with an assumed pH of 7.0 for sea salt particles, are about three orders of magnitude larger than the gas-to-particle mass transfer rates; thus the uptake of SO_2 by sea salt is rate limited by gas-to-particle transfer.

[46] Predicted annual mean mixing ratios of sulfate associated with sea salt are given in Figure 9a for the surface layer. Concentrations exceeding 100 pptv are found near the coastal regions where SO_2 concentrations exceed those in other parts of the oceans. The global mean mixing ratio of nss-sulfate on sea salt particles is 25.3 pptv, which is 15% of the global mean mixing ratio of 164 pptv for nss-sulfate from three other processes, the direct emission as primary particles, the gas-phase reaction of SO_2 with OH, and the in-cloud oxidation of SO_2 by H_2O_2 and O_3 .

[47] To understand the relative importance of this nss-sulfate formation in sea salt particles, we show in Figure 9b the surface layer ratios of annual mean mixing ratios of nss-sulfate on sea salt to those of total nss- and nondust sulfate (nss-sulfate formed on sea salt plus sulfate from direct emissions, gas-phase reaction of SO_2 with OH, and in-cloud oxidation). Large fractions of nss-sulfate associated with sea salt are predicted over the South Pacific Ocean between the east and northeast coasts of Australia and the coast of Southern Chile, off the coasts of Tanzania and Mozambique, and in the coastal zones of Eastern China and Brazil; over 50% of nondust nss-sulfate is predicted to be produced from sea salt uptake of SO_2 in these regions. These results agree well with previous one-dimensional studies of marine nss-sulfate that did not consider mineral dust uptake of SO_2 . A fraction of 10–30% of nss-sulfate is predicted to be associated with sea salt in the North Atlantic Ocean in this work, which agrees closely with the fraction of 5–25% proposed by Sievering *et al.* [1991, 1992]. Gurciullo *et al.* [1999] showed by using a box model that as much as 50–75% of the nss-sulfate observed during the First Aerosol Characterization Experiment (ACE-1) measurement period is produced in sea salt aerosol water, while Mari *et al.* [1999] estimated based on aircraft soundings that 22–50% of nss-sulfate is produced by oxidation in sea salt particles during the ACE-1 Lagrangian B. ACE-1

experiments took place in the Southern Ocean south of Australia (135–160°E, 41–54°S), where we predict that 30–60% of nondust nss-sulfate is in sea salt particles, which is within the ranges predicted by Gurciullo *et al.* [1999] and Mari *et al.* [1999].

[48] Figure 9c shows the ratios of annual mean column burdens of nss-sulfate on sea salt to those of total nss- and nondust sulfate. On a column-integrated basis, sea salt uptake of SO_2 is predicted to be important over southern oceans at 30–70°S, where concentrations of sea salt and SO_2 from DMS oxidation are high; sulfate formation in water associated with sea salt generally accounts for 30–50% of nss- and nondust sulfate formation in this region.

5.1.2. Sea Salt Uptake of HNO_3

[49] Over the oceans, gas-phase H_2SO_4 and HNO_3 react with sea salt to form sodium sulfate and sodium nitrate, respectively, affecting the partition of NH_3 and HNO_3 between gas and aerosol phases. The global surface layer distribution of nitrate aerosol formed in the sodium-ammonium-chloride-sulfate-nitrate-water aerosol system is shown in Figure 10a. It should be noted that the nitrate concentrations shown in Figure 10a do not include nitrate associated with dust particles since mineral dust aerosol is considered to be externally mixed with other aerosols. As expected, highest nondust nitrate concentrations are predicted over industrialized areas, with mixing ratios exceeding 1 ppbv over Europe, eastern United States, and eastern China. The effect of sea salt on nondust nitrate concentrations is shown in Figure 10b, which shows the differences between nitrate concentrations from the base case simulation with sea salt and those obtained in a sensitivity study with sea salt removed. Nitrate concentrations in the presence of sea salt generally increase by 100–1000 pptv along polluted coastal zones, resulting from the formation of sodium nitrate. Figure 10c presents the ratios of annual mean column burdens of nitrate predicted in the absence of sea salt to those obtained in the base case simulation. As expected, the model predicts higher nitrate burdens over the oceans in the presence of sea salt than in its absence. The formation of sodium nitrate leads to less gas-phase HNO_3 available for gas-aerosol partitioning over the continents, with nitrate burdens over United States, eastern China, and Europe reduced by 10–20% in the presence of sea salt. An area with high ratios of exceeding 1.6 is predicted to extend from North Africa to central Asia; however, nitrate concentrations predicted in this area in the base case simulation are in the range of 0–3 pptv (Figure 10a).

5.2. Influence of Mineral Dust on Concentrations of Sulfate and Nitrate

5.2.1. Predicted Dust Alkalinity

[50] Dust alkalinity is a key variable in determining the dust uptake of SO_2 and HNO_3 . We have assumed that dust alkalinity is contributed by the calcium ion and that the uptake of SO_2 and HNO_3 occurs when $[\text{Ca}^{2+}] -$

Figure 9. (a) Predicted annual mean mixing ratios (pptv) of sulfate associated with sea salt at the surface layer. Above the panel the global mean mixing ratio is indicated. Note that $1 \mu\text{g m}^{-3} \text{SO}_4^{2-} = 258 \text{ pptv SO}_4^{2-}$ at 298 K and 1000 mbar. (b) Ratios of annual mean mixing ratios of nss-sulfate on sea salt to those of total nss- and nondust sulfate (nss-sulfate formed on sea salt plus sulfate from direct emissions, gas-phase reaction of SO_2 with OH, and in-cloud oxidation) at the surface layer. (c) Ratios of annual mean column burdens of nss-sulfate on sea salt to those of total nss- and nondust sulfate.

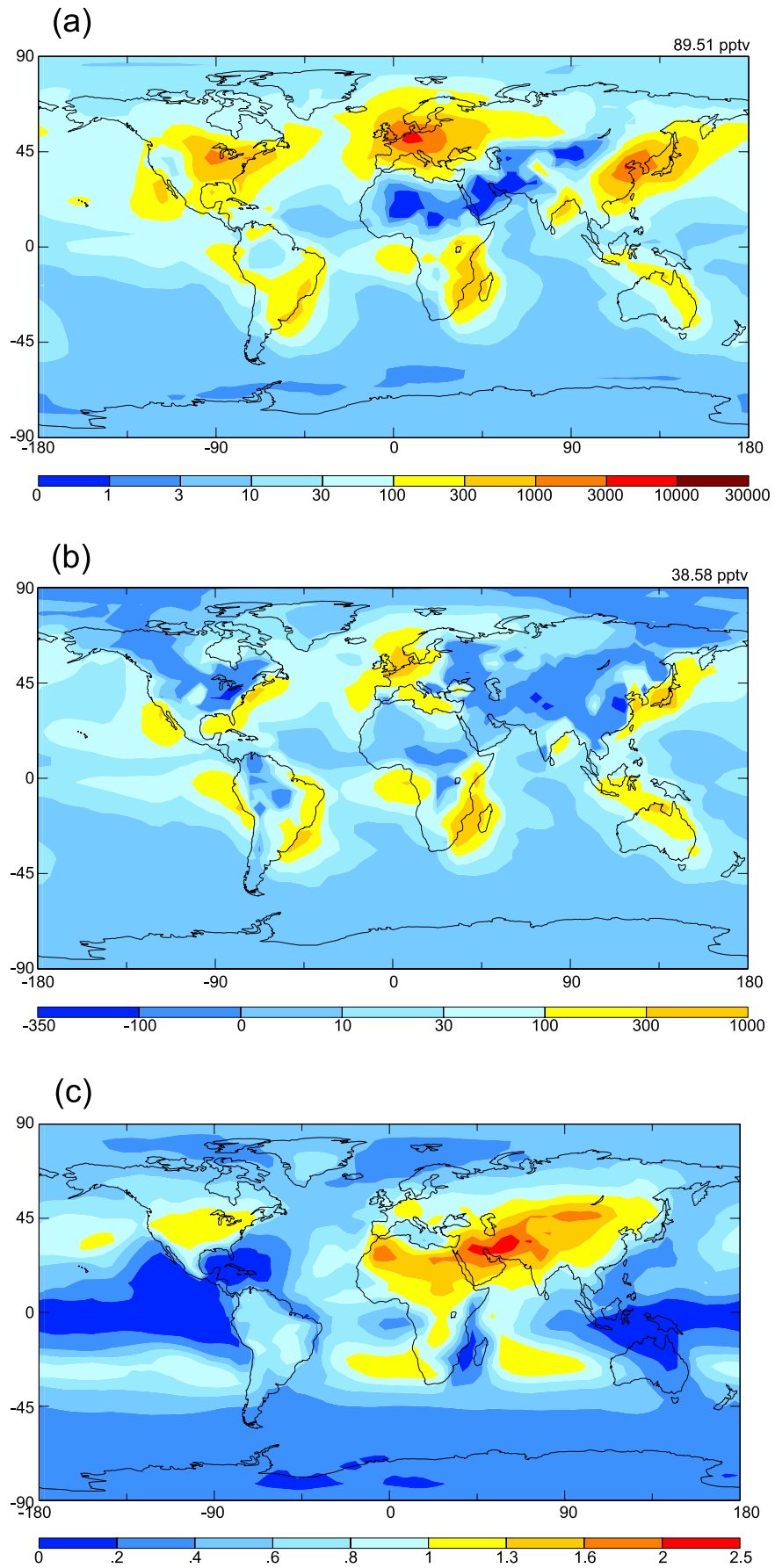


Figure 10

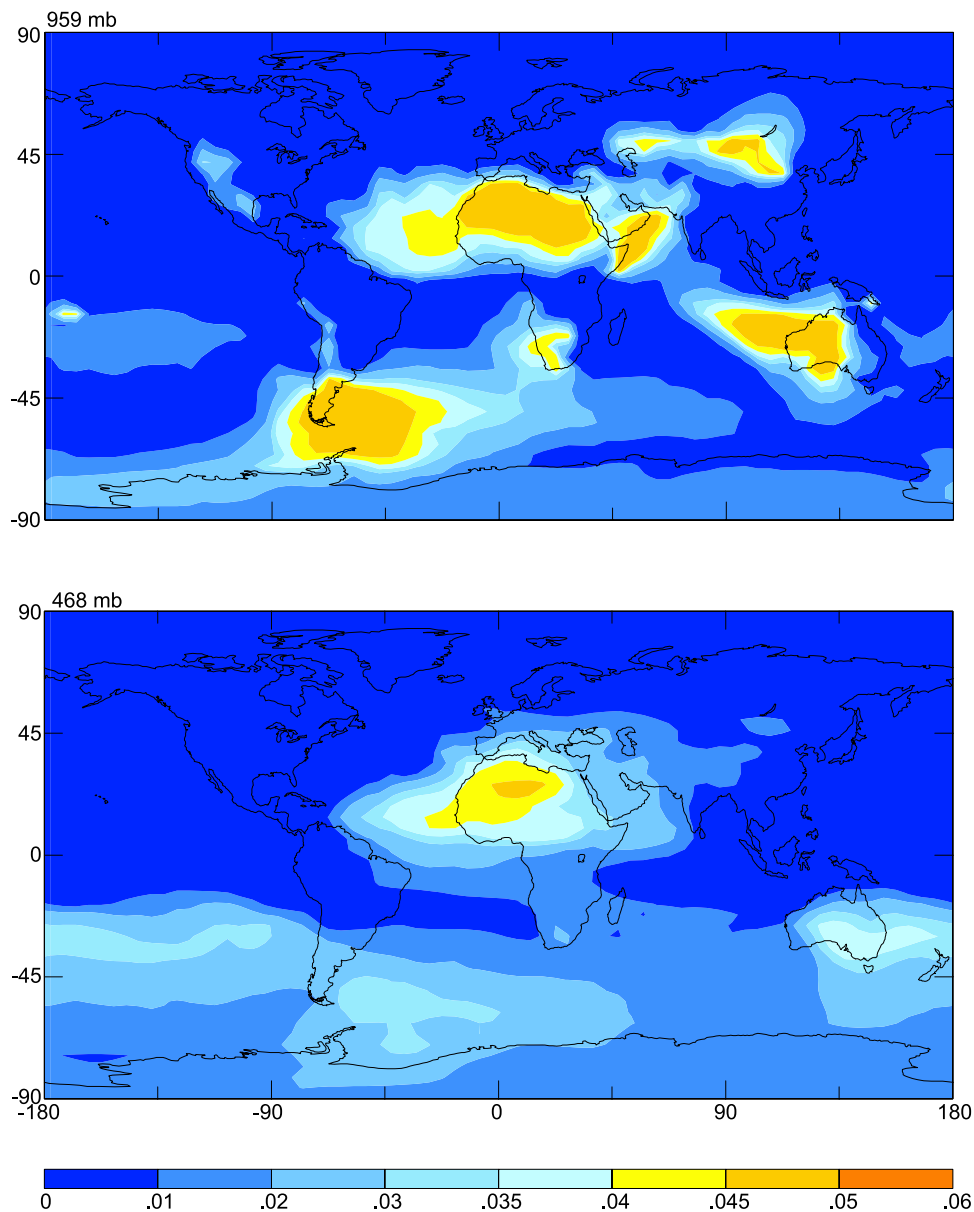


Figure 11. Ratios of annual mean *AlkCa* mass concentrations to annual mean concentrations of total dust mass at the surface layer and at 468 mbar altitude. Above each panel the pressure level of the GCM layer is indicated.

$[\text{SO}_4^{2-}(\text{dust})] - 0.5[\text{NO}_3^-(\text{dust})] > 0$. By treating *AlkCa*, the mass of Ca^{2+} that is not neutralized by dust associated SO_4^{2-} and NO_3^- , as a tracer, we are able to predict the change of dust alkalinity during dust transport. Figure 11 shows the ratios of annual mean *AlkCa* mass concentrations to annual mean concentrations of total dust mass at the surface layer and at 468 mbar altitude. At the surface layer, the ratios are close to 0.05 near dust sources since it is assumed that the Ca^{2+} content of freshly emitted dust is 5% by weight. The

ratios generally become smaller when dust particles are transported out of the source regions, because of titration from uptake of SO_2 and HNO_3 . However, the ratios are still higher than 0.045 in the dust plumes from the Patagonian Desert of southern Argentina and from Australia. Gas-phase HNO_3 and SO_2 concentrations in those two locations are not high enough to neutralize dust particles quickly. Dust particles also take up HNO_3 and SO_2 when they are transported vertically; the ratios at 468 mbar altitude are generally

Figure 10. (a) Predicted annual mean mixing ratios (pptv) of surface layer nitrate aerosol formed in the sodium-ammonium-chloride-sulfate-nitrate-water aerosol system. Note that $1 \mu\text{g m}^{-3} \text{NO}_3^- = 400 \text{ pptv NO}_3^-$ at 298 K and 1000 mbar. (b) Differences in nitrate concentrations (pptv) between the base case simulation with sea salt and a sensitivity study with sea salt removed. (c) Ratios of annual mean column burdens of nitrate predicted in the absence of sea salt to those obtained in the base case simulation. The global mean mixing ratio is indicated above Figures 10a and 10b.

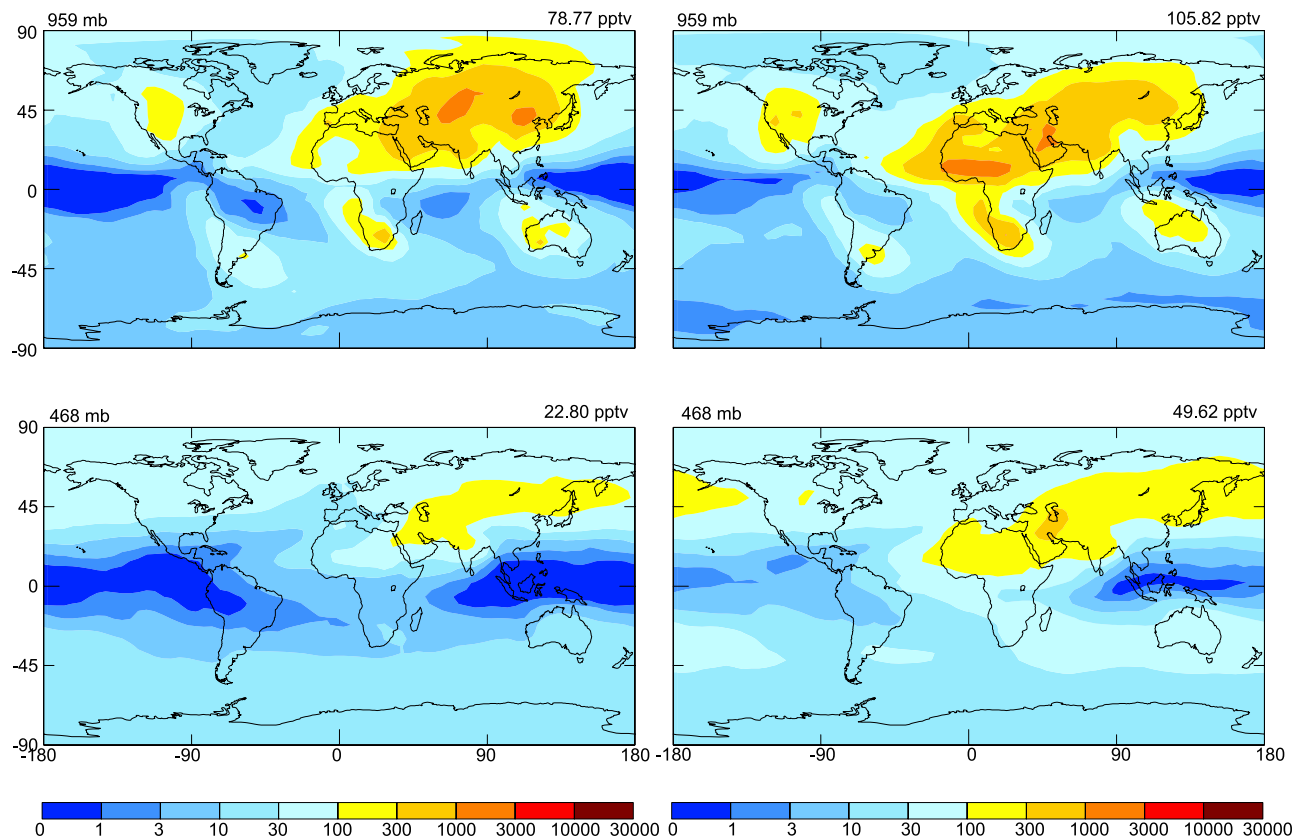


Figure 12. Annual mean mixing ratios (pptv) of sulfate and nitrate associated with mineral dust for surface layer and 468 mbar altitude. Above each panel the pressure level of the GCM layer is indicated, as is the average mixing ratio for that layer.

less than 0.04 except over the Sahara where dust emissions are strongest. In the middle troposphere, all dust particles over western United States are neutralized and dust particles over central Asia have only very weak alkalinity as a result of gas uptake.

5.2.2. Dust Uptake of SO_2 and HNO_3

[51] Annual mean mixing ratios of dust surface sulfate and nitrate produced from dust uptake of SO_2 and HNO_3 , respectively, are shown in Figure 12 for the surface layer and 468 mbar altitude. Highest mixing ratios are found near dust sources with available SO_2 and HNO_3 . Dust surface sulfate and nitrate mixing ratios exceeding 1 ppbv are predicted mainly over central Asia where dust emissions are strong while SO_2 and HNO_3 concentrations are high as a result of the transport from Europe. Such large mixing ratios of nitrate are also predicted over the biomass burning regions where HNO_3 concentrations are high. Compared with the mixing ratios of dust associated sulfate and nitrate shown in *Liao et al.* [2003], based on off-line dust concentrations and dust deposition, the on-line simulation in this work produces similar distributions but predicts more uptake of both SO_2 and HNO_3 at the surface layer. On a global mean basis, the concentrations of dust associated sulfate and nitrate in the surface layer are 79 and 106 pptv, respectively, about 5–15% higher than those obtained in *Liao et al.* [2003]. Some differences in the distributions of dust-associated sulfate and nitrate between this work and *Liao et al.* [2003] are found at 468 mbar. To estimate dust alkalinity,

Liao et al. [2003] assumed that the mass of dust deposited was simply balanced by an influx of fresh dust and scaled the off-line total deposition at the surface to all grid cells above it, which overestimated the deposition in the middle and upper troposphere.

[52] The simulated annual budget of HNO_3 is presented in Figure 13. Gas-to-particle conversion, dry deposition, and wet scavenging account for 48%, 22%, and 30% of HNO_3 removal, respectively. The calculated burden of

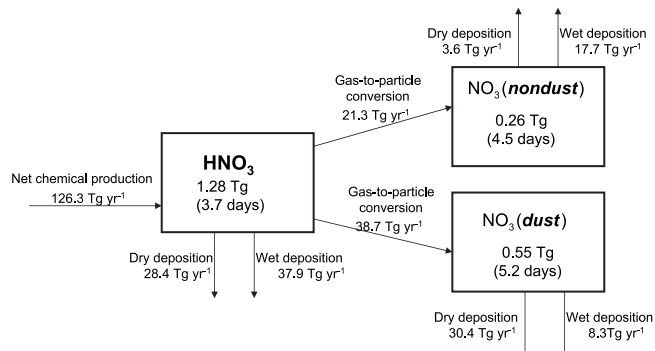


Figure 13. Global and annual average HNO_3 budget. Arrows indicate net fluxes. Burdens and lifetimes of gas-phase HNO_3 , nondust nitrate, and dust-associated nitrate are shown in their respective boxes.

Table 5. Comparison of Simulated and Observed nss SO₄²⁻ and NO₃ Concentrations in Marine Areas^a

| Location | Longitude | Latitude | Year | Time Period | nssSO ₄ ²⁻ | | | NO ₃ | | | Reference | | | | |
|--|-----------|---------------|----------------------|------------------------|----------------------------------|-----------------------------|----------|-----------------|-----------|-------|-----------|---------|-----------------------------|----------------------------|-----------------------------|
| | | | | | Measured | Predicted | | Measured | Predicted | | | | | | |
| | | | | | | OH + SO ₂ Clouds | Sea Salt | | Dust | Total | | NonDust | Dust | Total | |
| Southern Ocean south of Australia Indian Ocean | 135–160 E | 41–54 S | 1995 | November– December, | 0.216 | 0.110 | 0.059 | 0.038 | 0.207 | 0.01 | 0.050 | 0.106 | 0.156 | <i>Quinn et al.</i> [1998] | |
| | 30–54 E | 34–22 S | 1995 | March, | 0.22 | 0.106 | 0.104 | 0.136 | 0.346 | 0.22 | 0.062 | 0.037 | 0.099 | | <i>Rhoads et al.</i> [1997] |
| | 51–54 E | 18–6 S | 1995 | April | 0.36 | 0.099 | 0.011 | 0.012 | 0.122 | 1.01 | 0.056 | 0.021 | 0.077 | | |
| | 52–60 E | 6 S–6 N | 1995 | April | 1.4 | 0.102 | 0.009 | 0.028 | 0.139 | 1.71 | 0.170 | 0.281 | 0.451 | | <i>Quinn et al.</i> [2001] |
| | 60–80 E | 4.5–9 N | 1995 | April | 2.68 | 0.538 | 0.053 | 0.111 | 0.702 | 2.34 | 1.537 | 0.138 | 1.675 | | |
| | 76–66 W | 37–31 N | 1999 | January– February, | 2.49 | 3.15 | 0.860 | 0.085 | 4.095 | 0.235 | 0.029 | 0.207 | 0.236 | | |
| 66–43 W | 31–16 N | 1999 | January– February | 0.15 | 0.357 | 0.149 | 0.124 | 0.630 | 0.81 | 0.015 | 0.893 | 0.908 | | | |
| 43–33 W | 16–8 N | 1999 | January– February | 0.59 | 0.319 | 0.019 | 0.251 | 0.589 | 1.33 | 0.006 | 0.230 | 0.236 | | | |
| 33–26 W | 8–3 N | 1999 | January– February | 0.97 | 0.301 | 0.013 | 0.101 | 0.415 | 0.95 | 0.008 | 0.078 | 0.086 | | | |
| 26–17 W | 5S–3 N | 1999 | January– February | 1.13 | 0.06 | 0.015 | 0.038 | 0.113 | 0.19 | 0.006 | 0.245 | 0.251 | | | |
| 17 W–6 E | 25–5 S | 1999 | January– February | 0.57 | 0.1 | 0.024 | 0.154 | 0.278 | 0.14 | 0.017 | 0.537 | 0.554 | | | |
| 6–18 E | 33–25 S | 1999 | January– February | 0.59 | 0.166 | 0.033 | 0.324 | 0.523 | 0.59 | 0.232 | 0.100 | 0.332 | <i>Savoie et al.</i> [2002] | | |
| 59.4 W | 13.2 N | 1988– 1990 | February– annual | 0.84 | 0.387 | 0.155 | 0.116 | 0.658 | 1.09 | 0.533 | 0.233 | 0.766 | | | |
| 64.9 W | 32.3 N | 1988– 1990 | annual | 2.54 | 1.112 | 0.108 | 0.056 | 1.276 | 0.74 | 0.720 | 0.106 | 0.826 | <i>Savoie et al.</i> [2002] | | |
| 9.9 W | 53.3 N | 1989– 1990 | annual | 1.29 | 1.136 | 0.326 | 0.111 | 1.573 | 0.79 | 0.153 | 1.382 | 1.535 | | | |
| 16.5 W | 28.3 N | 1989– 1993 | annual | 0.992 | 0.837 | 0.166 | 0.527 | 1.530 | 0.114 | 0.017 | 0.008 | 0.025 | <i>Savoie et al.</i> [2002] | | |
| 170.6 W | 14.3 S | 1983– 1992 | annual | 0.371 | 0.018 | 0.009 | 0.006 | 0.033 | 0.29 | 0.121 | 0.043 | 0.164 | | | |
| 157 W | 71 N | 1997–2000 | annual | 0.43 | 0.519 | 0.024 | 0.114 | 0.657 | 0.29 | 0.121 | 0.043 | 0.164 | <i>Quinn et al.</i> [2002] | | |
| 177.2 W | 28.1 N | 1981–2000 | annual | 0.56 | 0.116 | 0.065 | 0.050 | 0.231 | 0.29 | 0.121 | 0.043 | 0.164 | | | |

^aUnits are in $\mu\text{g m}^{-3}$.

HNO_3 is 1.28 Tg, which is smaller than the 2.1 Tg reported by *Bauer et al.* [2004]. The discrepancy can be explained by the fact that nonmethane hydrocarbon chemistry and formation of nondust nitrate are not included in the work of *Bauer et al.* [2004]. Estimated burdens of nondust nitrate and dust surface nitrate are 0.26 and 0.55 Tg with lifetimes of 4.5 and 5.2 days, respectively. Slightly longer lifetime of nitrate associated with dust results because wet scavenging of dust is not as efficient as that of nondust nitrate.

5.3. Comparisons Between Measured and Simulated nss-SO₄²⁻ and NO₃⁻ Over Oceans

[53] We compare predicted concentrations of nss-SO₄²⁻ and NO₃⁻ with measurements in marine areas at selected sites (Table 5). Nss-SO₄²⁻ and NO₃⁻ are generally measured by extracting collected aerosols with water and analyzing the soluble SO₄²⁻ and NO₃⁻ by ion chromatography; thus, measured nss-SO₄²⁻ includes sulfate formed in water associated with sea salt, sulfate from direct emissions, gas-phase reaction of SO₂ with OH, and in-cloud oxidation, as well as sulfate formed on dust particles. Measured NO₃⁻ includes that associated with both the sodium-ammonium-chloride-sulfate-nitrate-water aerosol system and dust. The calculated contributions to the nss-SO₄²⁻ and NO₃⁻ concentrations by different processes are also listed in Table 5. It should be noted that among the measurements shown in Table 5, the concentrations from the studies of *Quinn et al.* [1998], *Rhoads et al.* [1997], and *Quinn et al.* [2001] were gathered over only relatively short periods, usually a few days or weeks, and strongly reflect the prevailing meteorological conditions. One must bear this in mind when comparing these data with GCM-simulated concentrations, which are based on climatological meteorology.

[54] Predicted nss-SO₄²⁻ concentration of 0.207 $\mu\text{g m}^{-3}$ agrees closely with measured 0.216 $\mu\text{g m}^{-3}$ obtained in the Southern Ocean region south of Australia during November and December of 1995. In this area, sea salt and dust uptake of SO₂ explains 29% and 18% of nss-SO₄²⁻ formation, respectively. Over the Indian Ocean, Nss-SO₄²⁻ and nitrate concentrations are significantly underestimated in the area that covers 52–60°E and 6°S–6°N, because very low concentrations of gas-phase SO₂ and HNO₃ are predicted there.

[55] Over the Atlantic Ocean, most predicted total sulfate and total nitrate concentrations are within a factor of 3 of ship measurements of *Quinn et al.* [2001], which took place during January and February of 1999. We underestimate both sulfate and nitrate in the area that crosses the equator (26–17°W, 5°S–3°N) by about 90%. Other measurements over Atlantic Ocean (Barbados (13.2°N, 59.4°W), Bermuda West (32.3°N, 64.9°W), Mace Head (53.3°N, 9.9°W), and Izana (28.3°N, 16.5°W)) and measurements over Pacific Ocean (American Samoa (14.3°S, 170.6°W), Midway Island (71°N, 157°W), and Barrow, Alaska (28.1°N, 177.2°W)) have been averaged over several years (see Table 5 for time periods these measurements were made). The predicted total sulfate and total nitrate are within a factor of 3 of observations at eighty-five percent of these stations.

[56] For the comparisons shown in Table 5, predicted total nss-SO₄²⁻ has a normalized mean error of 58.5% and a normalized mean bias of –23.4%, while predicted total

nitrate has a normalized mean error of 58.0% and a normalized mean bias of –33.3%. Negative normalized mean bias for both nss-SO₄²⁻ and nitrate indicates that the model tends to underestimate the concentrations of these two aerosols over the areas where the measurements were taken. Table 5 also shows that significant amounts of sulfate and nitrate are associated with mineral dust. Although we can compare predicted total sulfate and total nitrate mass concentrations with measurements, the fractions of sulfate and nitrate that are associated with dust can not be evaluated because of the lack of such specific measurements.

6. Direct Radiative Forcing

[57] Radiative forcing calculations are performed on-line within the GCM. The GISS radiation scheme uses the single Gauss point doubling/adding radiative transfer model [*Lacis and Hansen, 1974; Hansen et al., 1983; Lacis and Mishchenko, 1995*]. It uses the correlated *k*-distribution method to compute absorption by gases for 6 solar and 25 thermal intervals [*Lacis and Oinas, 1991*]. Radiative forcing is calculated as the difference in the net fluxes at the top of the atmosphere (TOA) and at the Earth's surface. We calculate the shortwave forcing by ozone, sulfate, nitrate, black carbon, organic carbon, sea salt and mineral dust, as well as the longwave radiative forcing by ozone and mineral dust aerosol. Aerosol radiative forcing by each aerosol species, as well as the total forcing by mixed aerosols, will be examined. The radiative forcing calculations are performed every 5 hours and do not feed back into the GCM climate.

6.1. Optical Properties of Each Aerosol Species

[58] Aerosol optical properties (extinction cross section, single-scattering albedo, and asymmetry parameter) are calculated by Mie theory based on wavelength-dependent refractive indices and aerosol size distributions. The effective dry radius and density, as well as optical properties of dry particles at $\lambda = 550$ nm, are listed in Table 6 for each aerosol class. The particle size distributions for black carbon, organic carbon, and sulfate aerosol that is not associated with dust and sea salt particles are assumed to obey the standard gamma distribution, with an area-weighted effective variance of 0.2 [*Chung and Seinfeld, 2002*]. Sulfate aerosol is represented optically as ammonium sulfate, with refractive indices from the work of *Toon et al.* [1976]. Refractive indices of soot are taken from the work of *d'Almeida et al.* [1991]. In the absence of data for organic carbon aerosol, refractive indices of "water-soluble" aerosol from the work of *d'Almeida et al.* [1991] are used for OC.

[59] Sea salt and mineral dust aerosol optical properties are calculated over each size bin, based on the parameters listed in Table 6. Then the overall extinction cross section σ , single-scattering albedo ω , and asymmetry parameter *g* of sea salt (or dust) are calculated by assuming sea salt (or dust) particles from different size bins are externally mixed. Wavelength-dependent refractive indices of sea salt are taken from *Volz* [1972], and those of mineral dust follow those used in *Liao and Seinfeld* [1998].

[60] We calculate nitrate optical properties over land and ocean differently. Over land, we assume that nitrate aerosol obeys the standard gamma distribution, with the same

Table 6. Aerosol Physical and Optical Properties at $\lambda = 550$ nm Assumed for Dry Aerosols^a

| Aerosol Type | r_{e_s} , μm | v_e | ρ , g cm^{-3} | σ_{e_s} , $\text{m}^2 \text{g}^{-1}$ | ω | g | Refractive Index | |
|--------------|---------------------------|-------|-----------------------------|---|----------|-------|--------------------|-------------------|
| Sulfate | 0.3 | 0.2 | 1.8 | 4.18 | 1.0 | 0.69 | $1.53 - 10^{-7} i$ | |
| OC | 0.5 | 0.2 | 1.8 | 2.46 | 0.96 | 0.67 | $1.53 - 0.004 i$ | |
| BC | 0.1 | 0.2 | 1.0 | 12.5 | 0.38 | 0.47 | $1.75 - 0.44 i$ | |
| Nitrate | 0.3 | 0.2 | 1.7 | 4.18 | 1.0 | 0.69 | $1.53 - 10^{-7} i$ | |
| Sea salt | 0.047 | | 2.25 | 0.12 | 1.0 | 0.056 | $1.50 - 10^{-8} i$ | |
| | 0.0965 | | 2.25 | 0.90 | 1.0 | 0.24 | $1.50 - 10^{-8} i$ | |
| | 0.19 | | 2.25 | 3.10 | 1.0 | 0.62 | $1.50 - 10^{-8} i$ | |
| | 0.375 | | 2.25 | 3.35 | 1.0 | 0.74 | $1.50 - 10^{-8} i$ | |
| | 0.75 | | 2.25 | 0.75 | 1.0 | 0.61 | $1.50 - 10^{-8} i$ | |
| | 1.5 | | 2.25 | 0.50 | 1.0 | 0.80 | $1.50 - 10^{-8} i$ | |
| | 3.0 | | 2.25 | 0.21 | 1.0 | 0.77 | $1.50 - 10^{-8} i$ | |
| | 6.0 | | 2.25 | 0.10 | 1.0 | 0.81 | $1.50 - 10^{-8} i$ | |
| | 12.0 | | 2.25 | 0.05 | 1.0 | 0.82 | $1.50 - 10^{-8} i$ | |
| | 24.0 | | 2.25 | 0.025 | 1.0 | 0.82 | $1.50 - 10^{-8} i$ | |
| | 48.0 | | 2.25 | 0.012 | 1.0 | 0.83 | $1.50 - 10^{-8} i$ | |
| | Dust | 0.065 | | 2.6 | 0.41 | 0.84 | 0.11 | $1.53 - 0.0078 i$ |
| | | 0.2 | | 2.6 | 3.43 | 0.97 | 0.64 | $1.53 - 0.0078 i$ |
| 0.65 | | | 2.6 | 0.86 | 0.85 | 0.52 | $1.53 - 0.0078 i$ | |
| 2.0 | | | 2.6 | 0.35 | 0.77 | 0.85 | $1.53 - 0.0078 i$ | |
| 6.5 | | | 2.6 | 0.094 | 0.60 | 0.93 | $1.53 - 0.0078 i$ | |
| | 21.0 | | 2.6 | 0.028 | 0.55 | 0.95 | $1.53 - 0.0078 i$ | |

^aHere r_{e_s} , effective dry radius; v_e , area-weighted effective variance; ρ , density; σ_{e_s} , extinction coefficient; ω , single-scattering albedo; g , asymmetry factor.

effective dry radius and area-weighted effective variance as those of sulfate aerosol (see Table 6), based on the urban measurements of *Lestari et al.* [2003]. Over the oceans, some fraction of nitrate is associated with coarse sea salt particles; hence the nitrate mass is distributed into each sea salt size bin proportionally to the aerosol surface area (or $A \times (\frac{R}{D_g} + \frac{4}{v\gamma})^{-1}$), where A is the total aerosol surface area in each sea salt size bin, R is the effective dry radius of sea salt, D_g is the gas-phase molecular diffusion coefficient of HNO_3 in air, v is the mean molecular speed, and γ is the uptake coefficient [Pandis et al., 1993; Lurmann et al., 1997]. Here a $\gamma(\text{HNO}_3)$ of 0.1 is used [Song and Carmichael, 2001]. Optical properties of nitrate over oceans are then calculated over each sea salt size bin using the effective dry radius of sea salt. Refractive indices of sulfate are used for nitrate aerosol [Sloane, 1983].

[61] Water uptake by each of sulfate, nitrate, and sea salt aerosols is determined by the aerosol thermodynamic equilibrium module, ISORROPIA, which uses the Zdanovskii-Stokes-Robinson (ZSR) correlation [Robinson and Stokes, 1965] to calculate the water content of the aerosols. Water uptake by organic carbon aerosol follows the treatment in the work of Chung and Seinfeld [2002]. Composite refractive indices of each aqueous aerosol are the volume-averaged refractive indices of the aerosol and water. Refractive indices of water are taken from the work of d'Almeida et al. [1991]. Mineral dust and black carbon are assumed to have no water uptake.

[62] Radiative forcing by sulfate and nitrate that is associated with dust can be neglected, because such sulfate and nitrate account for only a very small fraction of dust mass. We also neglect the forcing by sulfate formed in sea salt water, since most of such sulfate is associated with coarse particles.

6.2. Optical Properties of Mixed Aerosols

[63] In the aerosol population, we assume that sulfate, nitrate, black carbon, organic carbon, and sea salt aerosols

are internally mixed, leaving mineral dust externally mixed. Assuming that mineral dust is externally mixed with other aerosols is a reasonable first approximation because of the location of its principal source regions. We note, however, that there is evidence of internal mixing between elemental carbon and dust in Asian aerosols [Chuang et al., 2003]. The refractive indices of the internal mixture are calculated by volume-weighting the refractive indices of each aerosol species and water.

[64] Over land, where sea salt concentrations are low and sea salt particles surviving from long-distance transport are generally small, we assume that the internally mixed sulfate, nitrate, OC, BC, and sea salt aerosols have the standard gamma distribution, with an effective radius of 0.3 μm and an area-weighted effective variance of 0.2 [Chung and Seinfeld, 2002]. Over the oceans, sulfate, nitrate, OC, BC, sea salt, and aerosol water are assumed to be internally mixed within each sea salt size bin. Sulfate, OC, and BC are distributed into each sea salt bin according to their specified size distributions (see Table 6). Predicted nitrate associated with sea salt particles is distributed into each size bin as described in section 6.1. Aerosol water is allocated to each size bin using the same method as that used for the distribution of nitrate. For the calculation of optical properties over oceans, the effective dry radius of the internally mixed particles in each sea salt size bin is assumed to be that of sea salt.

6.3. Predicted Aerosol Optical Depth (AOD)

[65] Figure 14a shows the simulated annual mean global distribution of the column-integrated optical depth at the wavelength of 550 nm for mixed sulfate, nitrate, OC, BC, sea salt, mineral dust, and aerosol water. AODs of 0.5–0.7 are found over Europe, eastern Asia, and over the Sahara Desert. The highest AODs in Eastern North America are in the range of 0.3 to 0.4. Sea salt aerosol over the oceans around 60°S and 60°N generally has an optical depth of 0.2–0.4. On a global mean basis, mineral dust aerosol has

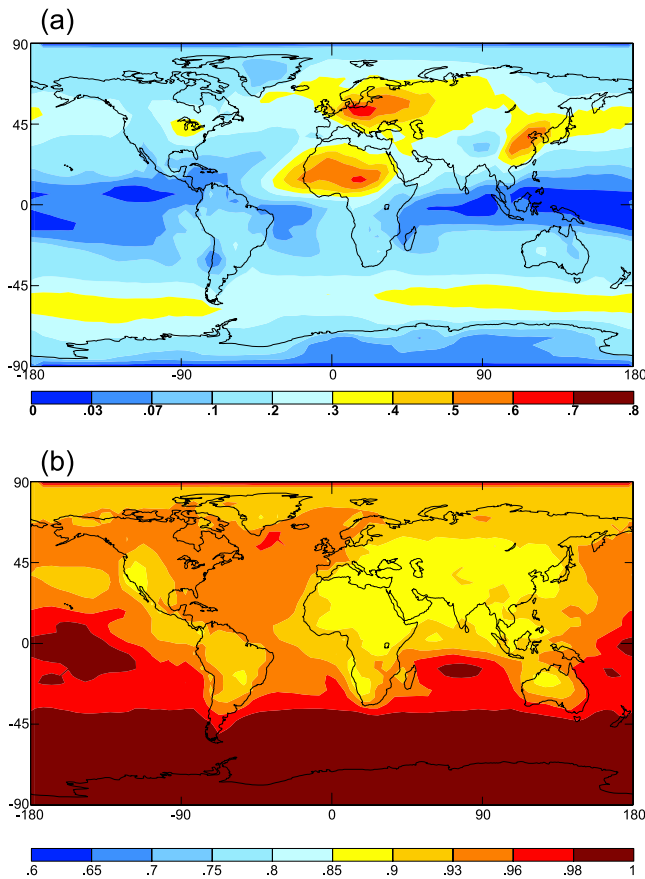


Figure 14. Simulated annual mean global distributions of (a) column-integrated aerosol optical depth and (b) single-scattering albedo at 550 nm for mixed sulfate, nitrate, OC, BC, sea salt, mineral dust, and aerosol water.

the largest individual optical depth of 0.037, followed by sulfate (0.024), sea salt (0.019), OC (0.012), nitrate (0.008), and BC (0.006).

[66] Predicted AODs of mixed aerosols with aerosol water are compared with the ground-based sun photometer measurements from AERONET [Holben *et al.*, 1998, 2001] in Figure 15. The AERONET program started in 1993, and has grown from about a dozen sites to over 100 sites worldwide. The period of AERONET measurements varies with the site, so we have chosen the sites that have quality assured data with two or more years of measurements available. It should be noted that AERONET measured column-integrated AODs are at 500 nm wavelength, whereas the predicted AODs are at 550 nm. Figure 15 also shows the simulated monthly mean optical depth of each aerosol species with water uptake.

[67] Figures 15(1) to 15(5) show the comparisons at sites in industrialized areas: Ispra (45.8°N, 8.6°E) and Venice (45.3°N, 12.5°E) in Europe, GSFC (Goddard Space Flight Center in Maryland, 39.0°N, 76.9°W), CART site (Cloud and Radiation Testbed in Oklahoma, 36.6°N, 97.4°W), and La Jolla (32.9°N, 117.3°W) in the United States. Modeled total AODs at Ispra, Venice, and CART site agree reasonably with measurements in both seasonal variation and magnitude. At each of these three

sites, sulfate is a major anthropogenic component. The model reproduces the AOD at La Jolla fairly well from November to May, but underestimates it by about 60% from June to August. At GSFC, the model does not capture the seasonal variation well; the predicted maximum AOD occurs in April while the measured one is in June–August.

[68] Figures 15(6) to 15(8) show the comparisons at three sites that are mainly influenced by organic carbon and black carbon aerosols from biomass burning. At Brazilia (15.9°S, 47.9°W) and Abracos Hill (10.8°S, 62.4°W) in Brazil, and Mongu (15.3°S, 23.2°E) in southern Africa, the GCM captures fairly well the seasonal variations. At each of these three sites, observations show a maximum AOD in September. Predictions also exhibit a peak at these locations, but the maximum AOD at Brazilia and Abracos Hill occurs in August. This difference in timing was also found by Takemura *et al.* [2002] and may be indicative of a difference between modeled and actual timing of burning. The model tends to underestimate the peak values; the predicted peak AODs at these three sites are about 60–70% of those observed.

[69] Figures 15(9) to 15(13) compare predicted and measured AODs at sites that are influenced mainly by mineral dust aerosol: Banizoumbou (13.5°N, 2.7°E) in northern Africa, Capo Verde (16.7°N, 22.9°W) off the west coast of northern Africa, Bahrain (26.3°N, 50.5°E) and Sede Boker (30.5°N, 34.5°E) in the Middle East, as well as Dalanzadgad (43.6°N, 104.4°E) in the Gobi Desert. The magnitude and seasonal variation of simulated AODs agree closely with those of observations at Banizoumbou and Bahrain. Predicted AODs at Sede Boker agree well with measurements from October to February, but the model overestimates optical depths in the other months. Model predictions are 48–68% higher than the measurements from March to September, except that predicted optical depth in April is about twice the observed value. The overestimation of AODs at Sede Boker possibly results from the overprediction of dust concentrations. At Capo Verde, the magnitude of predicted AOD agrees with that of the measurements throughout the year except in April. The model predicts a maximum in April but the observed peak is in June, which may arise from the GCM representation of winds used for the estimate of dust emission. At Dalanzadgad, the model reproduces the seasonal variation, but the model tends to overestimate AODs throughout the year. Predicted AODs at Dalanzadgad are close to the observed means plus one standard deviation from March to September, but simulated AODs in Northern Hemisphere winter are about twice the observed means, suggesting that the model may have overestimated Asian dust concentrations in winter.

[70] Comparisons shown in Figures 15(14) to 15(18) are for remote sites: Santiago (33.5°S, 70.7°W) in Chile, Barbados (13.2°N, 59.5°W) and Bermuda (32.4°N, 64.7°W) over Atlantic Ocean, Lanai (20.8°N, 157.0°W) in the middle of Pacific Ocean, and Anmyon Island (36.5°N, 126.3°E) in Korea. Predicted AODs at Santiago and Barbados are close to the lower limits of observations. Low AODs predicted at Barbados result from the underestimation of dust concentrations at this site. At

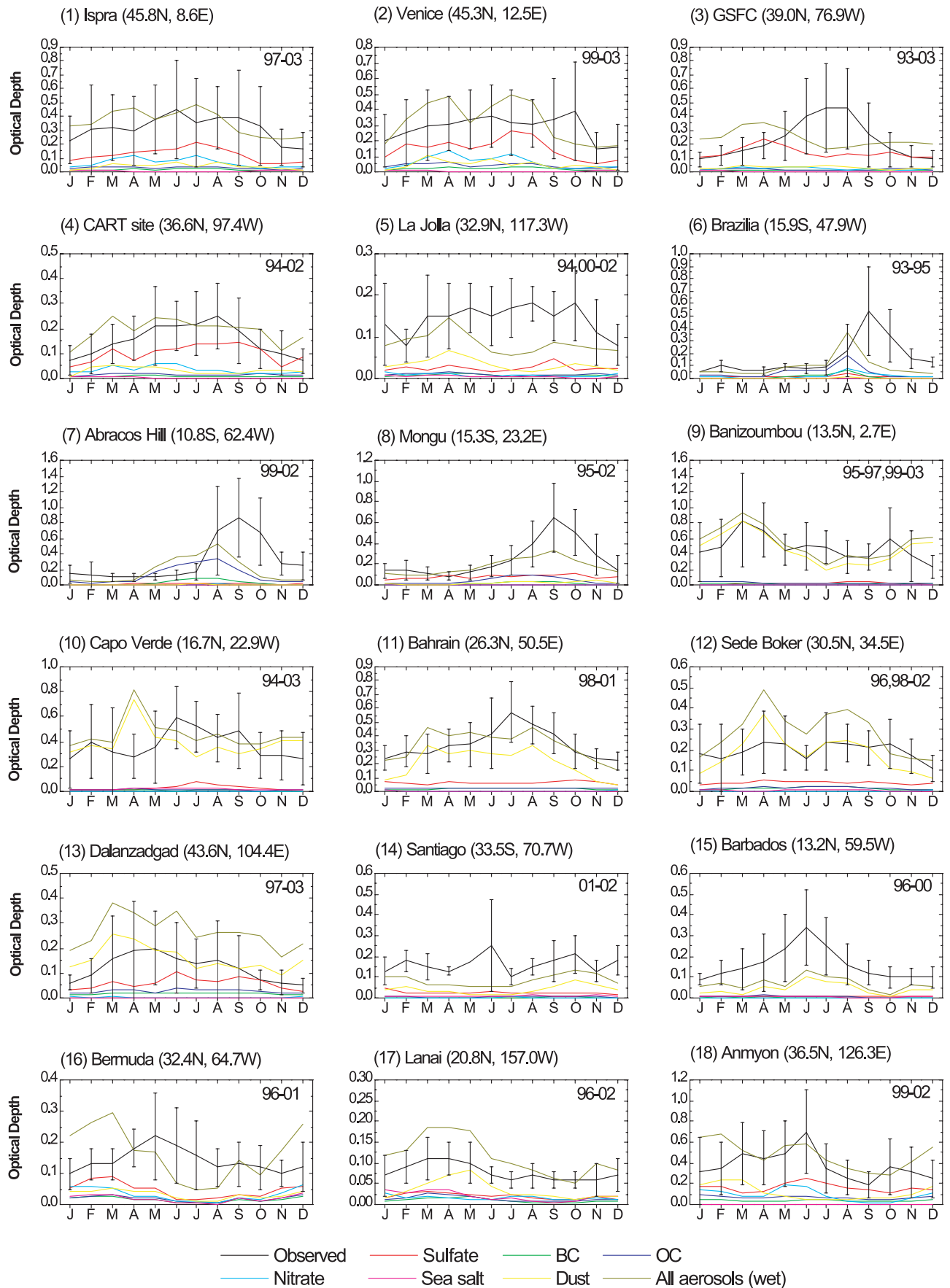


Figure 15

Table 7. Simulated and Observed Aerosol Single-Scattering Albedo^a

| Location | Longitude | Latitude | Time Period | Observed | Simulated | Reference |
|---|-----------|----------|-------------|-----------|-----------|--------------------------------|
| <i>Comparison With Surface Measurements</i> | | | | | | |
| Arctic | 62.5°W | 82.5°N | annual | 0.96 | 0.91 | Heintzenberg et al. [1997] |
| Ny Alesund | 12°E | 79°N | annual | 0.948 | 0.92 | Heintzenberg et al. [1997] |
| Spitsbergen | 12°W | 79°N | annual | 0.93–0.97 | 0.92 | Heintzenberg and Leck [1994] |
| Barrow | 156.3°W | 71.2°N | annual | 0.96 | 0.93 | Heintzenberg et al. [1997] |
| Stockholm | 18°E | 59.2°N | annual | 0.89 | 0.91 | Heintzenberg [1982] |
| Kamchatka | 160°E | 56°N | May | 0.88 | 0.93 | Clarke [1989] |
| Cheeka Peak | 124.6°W | 48.3°N | March | 0.85–0.97 | 0.97 | Anderson et al. [1999] |
| Sable Island | 60°W | 43.9°N | annual | 0.86–0.97 | 0.95 | Ogren et al. [1999] |
| Abastumani | 42.5°E | 41.4°N | annual | 0.89 | 0.90 | Heintzenberg et al. [1997] |
| Bondville | 88.4°W | 40.1°N | annual | 0.86–0.97 | 0.95 | Ogren et al. [1999] |
| Allegheny Mountains | 80°W | 38.3°N | August | 0.87 | 0.96 | Japar et al. [1986] |
| Shenandoah | 78°W | 38°N | July | 0.95 | 0.94 | Ferman et al. [1981] |
| TARFOX | 74°W | 37.5°N | August | 0.90 | 0.91 | Hegg et al. [1997] |
| Mesa Verde | 108.3°W | 37.1°N | annual | 0.91 | 0.90 | Heintzenberg et al. [1997] |
| Sagres | 9°W | 37°N | July | 0.94 | 0.89 | Carrico et al. [2000] |
| Oklahoma | 97.5°W | 36.6°N | annual | 0.92–0.99 | 0.93 | Ogren et al. [1999] |
| Anderson Mesa | 111.4° W | 35.1°N | annual | 0.94 | 0.89 | Heintzenberg et al. [1997] |
| Mauna Loa | 155.4°W | 19.3°N | annual | 0.97 | 0.96 | Bodhaine [1995] |
| Kaashidhoo | 73.5°E | 5.0°N | February | 0.87–0.9 | 0.89 | Satheesh and Ramanathan [2000] |
| Tropical Atlantic | 20°W | 5°S | August | 0.8 | 0.92 | Clarke [1989] |
| Cuiabá | 56°W | 16°S | August | 0.85 | 0.83 | Reid et al. [1998] |
| Amundsen Scott | | 90°S | annual | 0.965 | 0.99 | Heintzenberg et al. [1997] |
| <i>Comparison With AERONET Measurements</i> | | | | | | |
| Ispra | 8.6°E | 45.8°N | Aug.–Dec. | 0.94 | 0.94 | AERONET |
| GSFC | 76.9°W | 39.0°N | DJF | 0.92 | 0.94 | AERONET |
| | | | MAM | 0.93 | 0.94 | |
| | | | JJA | 0.96 | 0.94 | |
| | | | SON | 0.94 | 0.93 | |
| Lanai | 157.0°W | 20.8°N | DJF | 0.97 | 0.97 | AERONET |
| | | | MAM | 0.97 | 0.94 | |
| | | | JJA | 0.97 | 0.95 | |
| | | | SON | 0.96 | 0.96 | |
| Capo Verde | 22.9°W | 16.7°N | DJF | 0.96 | 0.92 | AERONET |
| | | | MAM | 0.96 | 0.92 | |
| | | | JJA | 0.98 | 0.94 | |
| | | | SON | 0.97 | 0.94 | |
| Banizoumbou | 2.7°E | 13.5°N | annual | 0.96 | 0.89 | AERONET |
| Los Fieros | 56°W | 14.6°S | June–July | 0.87 | 0.82 | AERONET |
| | | | Aug.–Oct. | 0.94 | 0.87 | |
| Mongu | 23.2E | 15.25 | JJA | 0.84 | 0.86 | AERONET |
| | | | SON | 0.91 | 0.90 | |

^aDJF, December–January–February; MAM, March–April–May; JJA, June–July–August; SON, September–October–November.

Bermuda and Lanai, dust aerosol is from the long-range transport from Africa and Asia, respectively. Predicted AODs at Lanai are higher than measured means plus one standard deviation from March to July. Although we do not have direct comparisons of simulated dust concentrations with measurements at Lanai, simulated dust concentrations agree with measurements at Oahu (21.3°N, 157.7°W) (see Figure 7), a site that is very close to Lanai; therefore the overestimation of March–April–May AODs at Lanai may arise from the overestimation of other aerosols. Predicted seasonal variation of AODs at Bermuda does not match the observed seasonal cycle. As discussed in section 4.2, the GCM may not

represent the circulation around Bermuda, which may have influenced the transportation of aerosols in this area. Predicted and observed AODs agree at Anmyon. A scatterplot (not shown) of all the data points used in Figure 15 indicates that 83% of model predicted monthly average AODs agree with AERONET measured values within a factor of 2.

6.4. Predicted Single-Scattering Albedo (SSA)

[71] Figure 14b shows the simulated annual mean global distribution of column-integrated SSA at 0.55 μm for mixed sulfate, nitrate, OC, BC, sea salt, mineral dust, and aerosol water. SSA over the North America is

Figure 15. Comparison of total aerosol optical depth of mixed sulfate, nitrate, OC, BC, sea salt, mineral dust, and aerosol water with that measured at 18 AERONET sites. Site location and the measurement period are indicated for each site. The error bar indicates one standard deviation of observed optical depth. Plots also show the simulated optical depth for each aerosol component.

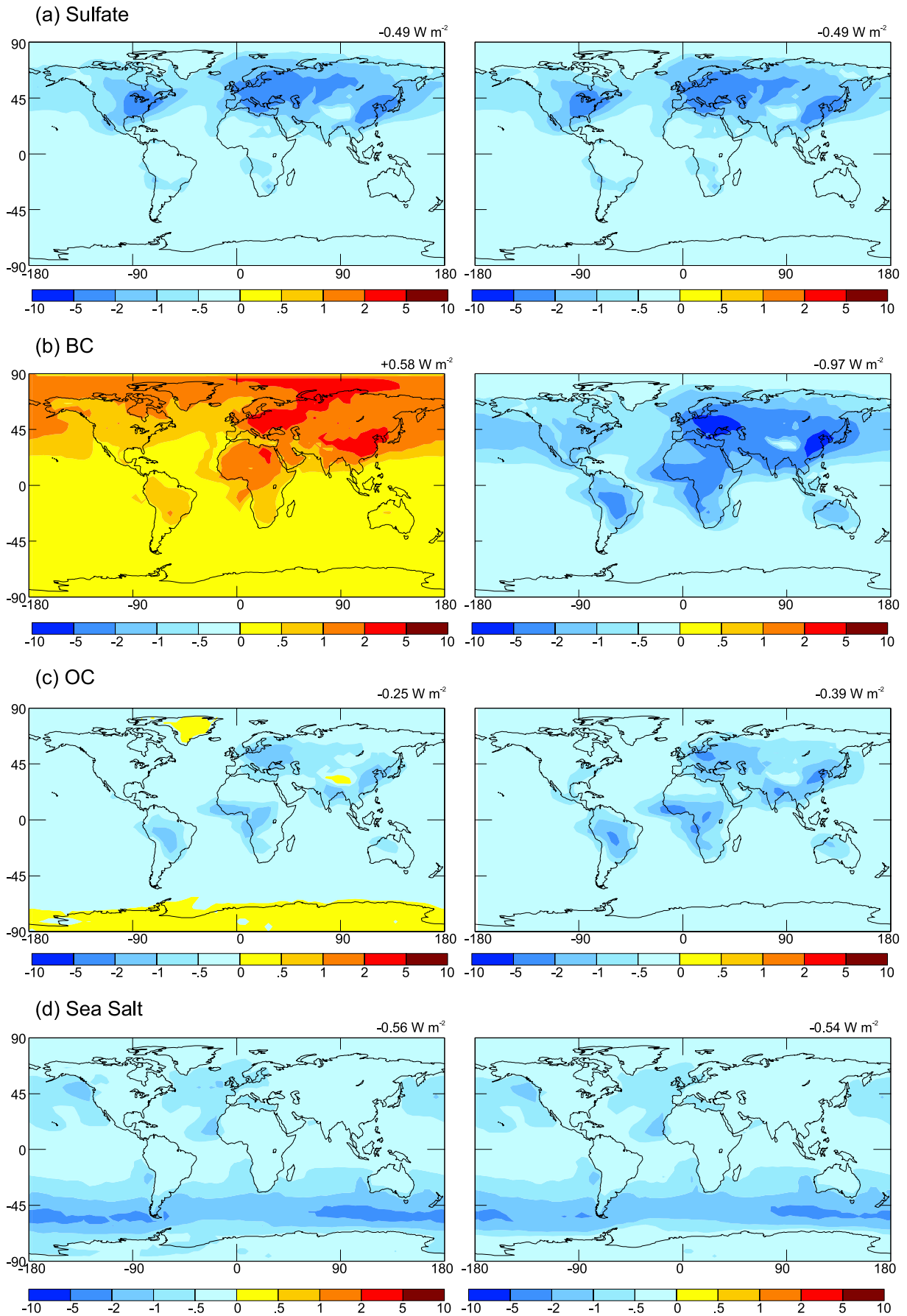


Figure 16

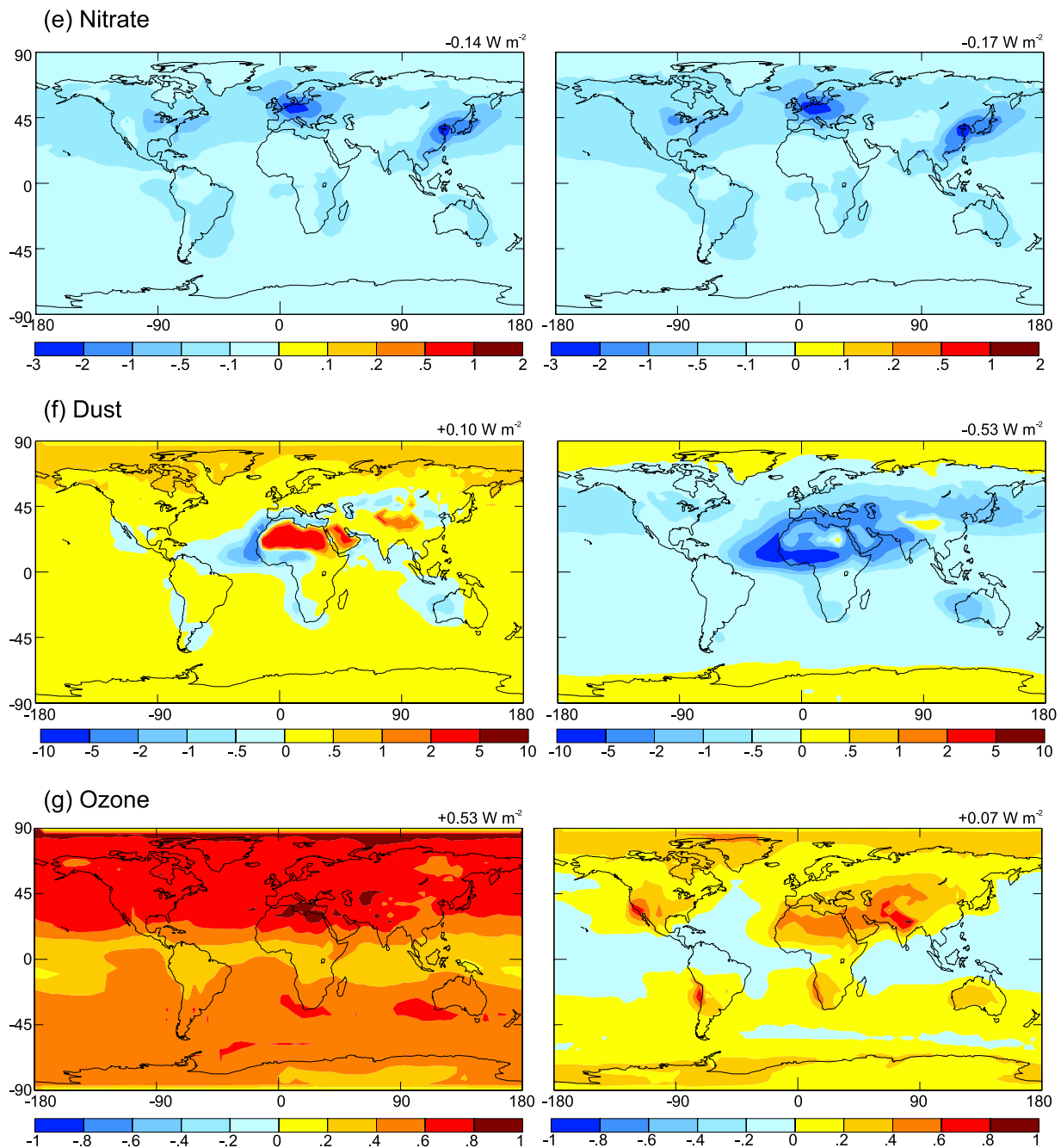


Figure 16. (continued)

generally in the range of 0.9 to 0.96, except that it is lower than 0.9 near the west coast where dust is present. Simulated SSA is in the range of 0.9–0.96 over Western Europe, whereas it is 0.85–0.9 in the eastern and downwind areas of Europe. Predicted SSAs over regions with mineral dust and biomass burning aerosols are generally lower than 0.9.

[72] Table 7 compares the simulated SSAs with both surface measurements and AERONET retrievals. For the comparisons with surface measurements, the SSAs of dry aerosols in the lowest GCM layer are used; most surface measurements were obtained from filter-based methods, which derive absorption from the change in light transmission through a filter on which particles have been collected

Figure 16. Annual mean distributions of the simulated TOA (left column) and surface (right column) radiative forcings by each of wet aerosol species: (a) sulfate, (b) BC, (c) OC, (d) sea salt, (e) nitrate, (f) mineral dust, and (g) tropospheric ozone. Both natural and anthropogenic aerosols and ozone are included in the calculations. Above each panel the global and annual mean forcing value is indicated.

Table 8. Global and Annual Mean TOA and Surface Radiative Forcing by Aerosols and/or O₃

| Species | TOA Forcing, W m ⁻² | Surface Forcing, W m ⁻² |
|---------------------------------|--|--|
| Sulfate | -0.49 | -0.49 |
| Black carbon | +0.58 | -0.97 |
| Organic carbon | -0.25 | -0.39 |
| Nitrate | -0.14 | -0.17 |
| Sea salt | -0.56 | -0.54 |
| Mineral dust | +0.10 (longwave +0.31, shortwave -0.21) | -0.53 (longwave +0.53, shortwave -1.06) |
| All aerosols | -0.72 | -4.04 |
| O ₃ | +0.53 (longwave +0.32, shortwave +0.21) | +0.07 (longwave +0.32, shortwave -0.25) |
| O ₃ and all aerosols | -0.46 | -3.74 |

[Bond *et al.*, 1999]. The column-integrated SSAs as shown in Figure 14b are used for the comparisons with AERONET measurements. The simulated SSAs have been averaged over the same time of year as measurements. Most simulated values at urban and remote sites agree closely with measurements. Predicted SSAs at Kamchatka, Allegheny Mountains, and the tropical Atlantic are considerably higher than the observed values, possibly caused by the errors in measurements [Ghan *et al.*, 2001]. At Banizoumbou where the dominant aerosol is dust, the predicted SSA is 0.89, which is much lower than the AERONET measured value of 0.96. Such a large discrepancy between predicted and measured SSA over dust regions was also reported by Takemura *et al.* [2002]. In their study predicted SSA values over dust regions were always less than 0.9, but AERONET measured values were all around 0.95. Since the calculated SSA based on measured refractive indices of dust is 0.86 [Carlson and Benjamin, 1980], these differences between calculated and AERONET measured SSA over dust regions require more investigation.

6.5. Radiative Forcing

6.5.1. TOA and Surface Forcing by Each Aerosol Component and Ozone

[73] Figure 16 shows the annual mean distributions of the simulated TOA and surface radiative forcing by each aerosol species and by O₃. Both the magnitude and distribution of sulfate forcing at TOA are similar to those at the surface. The global mean sulfate forcing at TOA is calculated to be -0.49 W m⁻², which agrees closely with the sulfate TOA forcing of -0.40 W m⁻² estimated by Takemura *et al.* [2002] and -0.44 W m⁻² by Jacobson [2001]. BC has high positive forcing at TOA and strong negative forcing at the surface because of its absorbing character and large mass extinction efficiency of 12.5 m² g⁻¹ (Table 6). TOA BC forcing exceeds +2 W m⁻² over areas with high BC concentrations from fossil consumption and biomass burning, and over areas with high surface albedo. The distribution of BC forcing at TOA differs from that at the surface; surface forcing is not strong over areas with high albedo because surface cooling depends only on absorption and scattering of BC. Surface BC cooling reaches a maximum of -9 W m⁻² over Europe and eastern China. The global and annual mean OC forcing is estimated to be -0.25 W m⁻² at TOA and -0.39 W m⁻² at the surface. Stronger cooling by OC at the surface than at TOA results from the weak absorption of OC, which was also found by Jacobson [2001].

[74] Sea salt and nitrate aerosols exhibit negative forcing globally at both TOA and surface, and the forcing values at TOA are about the same as those at the surface for each of these two aerosols. The global and annual mean radiative forcing by sea salt is -0.56 W m⁻², which is within the range of previous estimates. Global mean sea salt TOA forcing was calculated to be -0.31 W m⁻² in Takemura *et al.* [2002], whereas it was estimated to be -1.1 W m⁻² by Grini *et al.* [2002]. The largest forcing by sea salt is located around 60°S in the Southern Hemisphere, with maximum cooling reaching -2.4 W m⁻².

[75] Nitrate forcing is calculated to be the smallest among all the aerosol species. The global and annual mean forcing is -0.14 W m⁻² at TOA and -0.17 W m⁻² at the surface. The TOA nitrate forcing calculated here is between the -0.07 W m⁻² estimated by Jacobson [2001] and -0.3 W m⁻² reported by Adams *et al.* [2001].

[76] Dust forcing shown in Figure 16f is the sum of dust shortwave and longwave forcings. At TOA, strong heating exceeding +2.0 W m⁻² over the Sahara Desert results from the positive shortwave and longwave forcings there. Although TOA longwave forcing is always positive, the longwave forcing values are not large enough to offset the shortwave cooling over low albedo surfaces; the net TOA forcing off the west coast of North Africa still reaches -4.7 W m⁻². At the surface, strong shortwave cooling is offset by strong longwave heating, giving a modest forcing over deserts. The annual and global mean dust radiative forcing is predicted to be +0.10 W m⁻² (-0.21 shortwave plus +0.31 longwave) at TOA and -0.53 W m⁻² (-1.06 shortwave plus +0.53 longwave) at the surface. The global mean TOA dust forcing predicted here is between the -0.14 W m⁻² estimated by Jacobson [2001] and the +0.36 W m⁻² calculated by Takemura *et al.* [2002], and agrees closely with the value of +0.07 W m⁻² obtained by Woodward [2001]. The global mean surface dust forcing is smaller than the -0.85 and -0.82 W m⁻² calculated by Jacobson [2001] and Woodward [2001], respectively.

[77] Global and annual mean net TOA radiative forcing by tropospheric O₃ is estimated to be +0.53 W m⁻² (+0.21 W m⁻² from the shortwave and +0.32 W m⁻² from the longwave), which is about the same as the predicted global mean TOA forcing of BC. O₃ forcing is distributed more uniformly over lands and oceans in the mid to high latitudes of each hemisphere than BC forcing. High TOA O₃ forcing of about +1.0 W m⁻² at northern midlatitudes comes from longwave forcing as a result of the large temperature

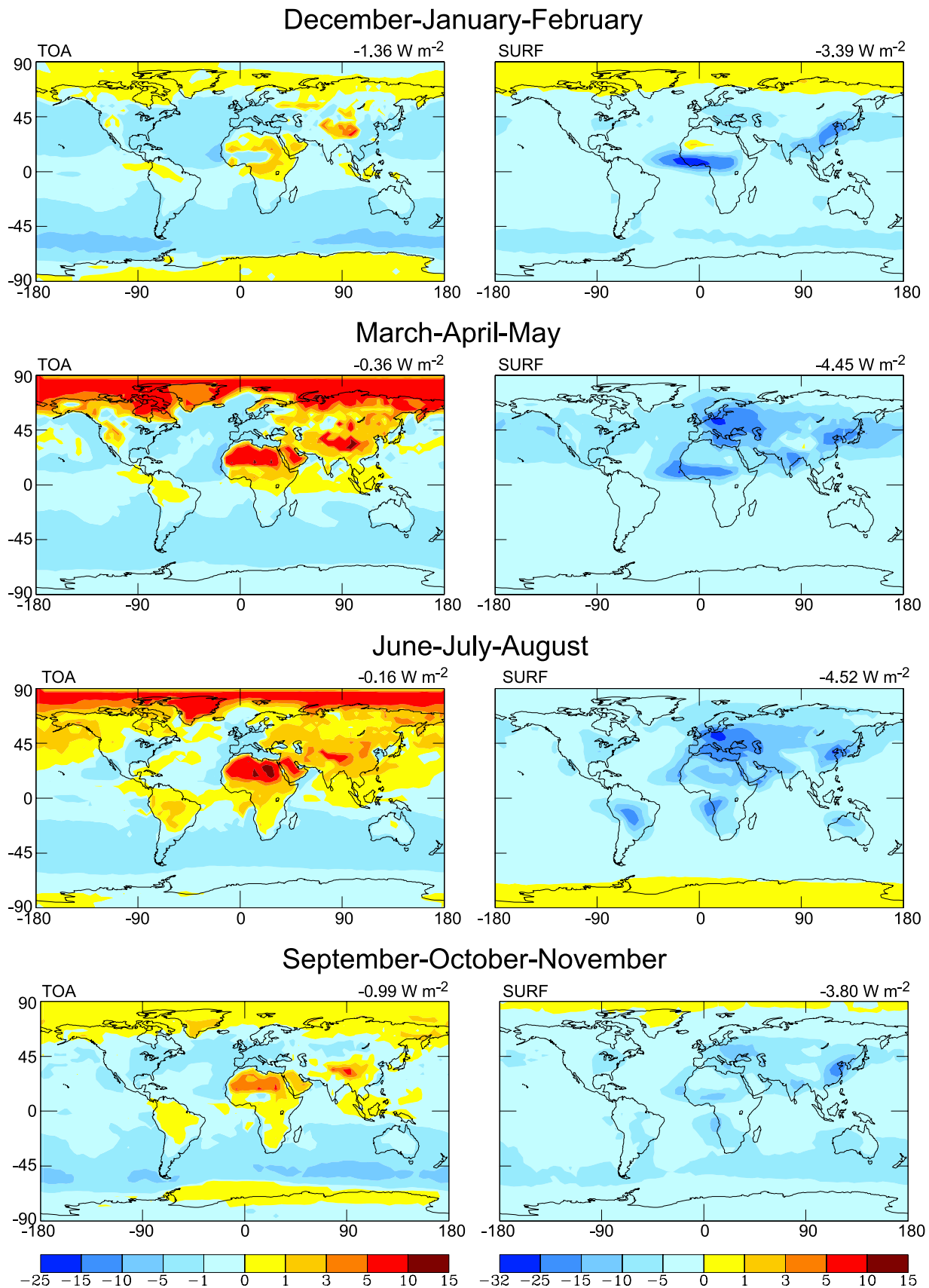


Figure 17. Predicted seasonal mean distributions of (left) TOA and (right) surface net (shortwave plus longwave) direct radiative forcing by mixed sulfate, nitrate, OC, BC, sea salt, mineral dust, and aerosol water. Above each panel the global and seasonal mean forcing value is indicated.

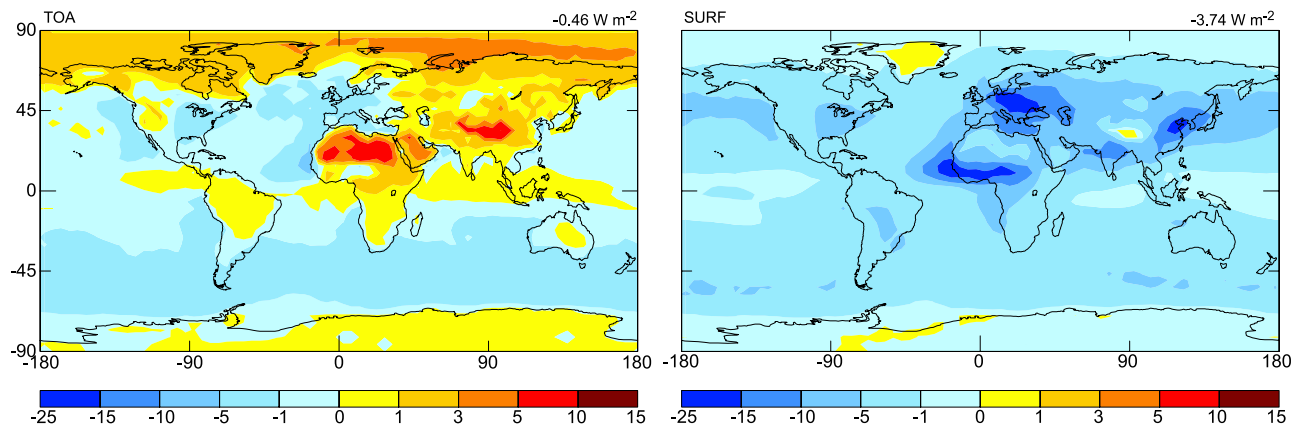


Figure 18. Predicted annual mean distributions of combined radiative forcing (W m^{-2}) by tropospheric ozone and mixed aerosols (sulfate, nitrate, OC, BC, sea salt, mineral dust, and aerosol water) at TOA and surface. Both natural and anthropogenic aerosols and ozone are included in the calculations. Above each panel the global and annual mean forcing value is indicated.

differences between the Earth's surface and TOA in these regions [Mickley *et al.*, 1999], and the high TOA O_3 forcing in the Arctic region results from the high albedo there that leads to more reflected sunlight to be absorbed by O_3 . At the surface, O_3 shortwave forcing is globally negative, which offsets the positive O_3 longwave forcing and leads to relatively small net forcings at the surface.

[78] The simulated global and annual mean radiative forcing values of each aerosol component and O_3 are summarized in Table 8. Aerosol surface forcing is always negative, with the magnitude of cooling depending on the aerosol absorption. BC produces the strongest cooling at the surface, followed by mineral dust and organic carbon.

6.5.2. Total Aerosol Forcing

[79] Figure 17 shows the simulated seasonal mean distributions of net (shortwave plus longwave) direct radiative forcing by mixed sulfate, nitrate, OC, BC, sea salt, mineral dust, and aerosol water. The global and annual mean forcing is calculated to be -0.72 W m^{-2} at TOA and -4.04 W m^{-2} at the surface. The global mean TOA forcing indicates strong cooling in SON (-0.99 W m^{-2}) and DJF (-1.36 W m^{-2}), and less cooling in MAM (-0.36 W m^{-2}) and JJA (-0.16 W m^{-2}) when heating by BC from industrial emissions and by dust are strongest. For the same reason, global and seasonal mean surface cooling is strongest in MAM and JJA. The magnitude of surface cooling is much larger than that of TOA forcing; while the largest cooling and heating at TOA are -10 and $+12 \text{ W m}^{-2}$, respectively, surface forcing is predicted to reach as high as -30 W m^{-2} over central Africa in DJF and over Europe in MAM and JJA. This large difference in the magnitudes of surface and TOA forcings is caused by absorption of BC, mineral dust, and OC aerosols and is supported by measurements. Based on simultaneous measurements at the Earth's surface and TOA over the tropical northern Indian Ocean, *Satheesh and Ramanathan* [2000] found that mean clear-sky solar radiative heating for the winters of 1998 and 1999 decreased at the ocean surface by 12 to 30 W m^{-2} , but only by 4 to 10 W m^{-2} at TOA. Recently, *Bush and Valero* [2003] reported that measured

diurnal average aerosol forcing at the surface ranged between -10.6 to -52.1 W m^{-2} on clear days at Gosan, Jeju, Republic of Korea, during the ACE-Asia field campaign.

6.5.3. Combined Forcing of Ozone and Aerosols

[80] Distributions of annual mean TOA and surface radiative forcings from tropospheric ozone and all aerosol species are shown in Figure 18. Since O_3 forcing is quite uniformly distributed at TOA and relatively small at the surface (Figure 16g), the distributions of combined O_3 and aerosol TOA and surface forcings are very similar to those of all aerosols (Figure 17). The combined global and annual average TOA and surface forcings are -0.46 and -3.74 W m^{-2} , respectively.

7. Effects of Coupling Between Gas-Phase Chemistry and Aerosols on Radiative Forcing Estimates

[81] The major couplings between gas-phase tropospheric chemistry and aerosols accounted for in this study are (1) hydrolysis of N_2O_5 on wet aerosol surfaces; (2) irreversible absorption of NO_3 , NO_2 , and HO_2 by wet

Table 9. Predicted Global and Annual Average Burdens in the Presence (Baseline) and Absence of Heterogeneous Reactions^a

| Species | No Heterogeneous Reactions | |
|--|----------------------------|--------------------------|
| | Baseline | |
| SO_2 | 0.47 | 0.58 (+23%) ^b |
| SO_4^{2-} (not associated with dust and sea salt) | 1.34 | 1.71 (+28%) |
| HNO_3 | 1.28 | 1.80 (+41%) |
| O_3 | 304 | 354 (+16%) |
| NH_3 | 0.23 | 0.20 (-13%) |
| NH_4^+ | 0.34 | 0.38 (+12%) |
| NO_3^- (not associated with dust) | 0.26 | 0.39 (+50%) |
| SO_4^{2-} (associated with sea salt) | 0.17 | 0. |
| SO_4^{2-} (associated with dust) | 0.30 | 0. |
| NO_3^- (associated with dust) | 0.55 | 0. |

^aUnits are in Tg .

^bNumbers in parentheses are percentage changes compared with the baseline case.

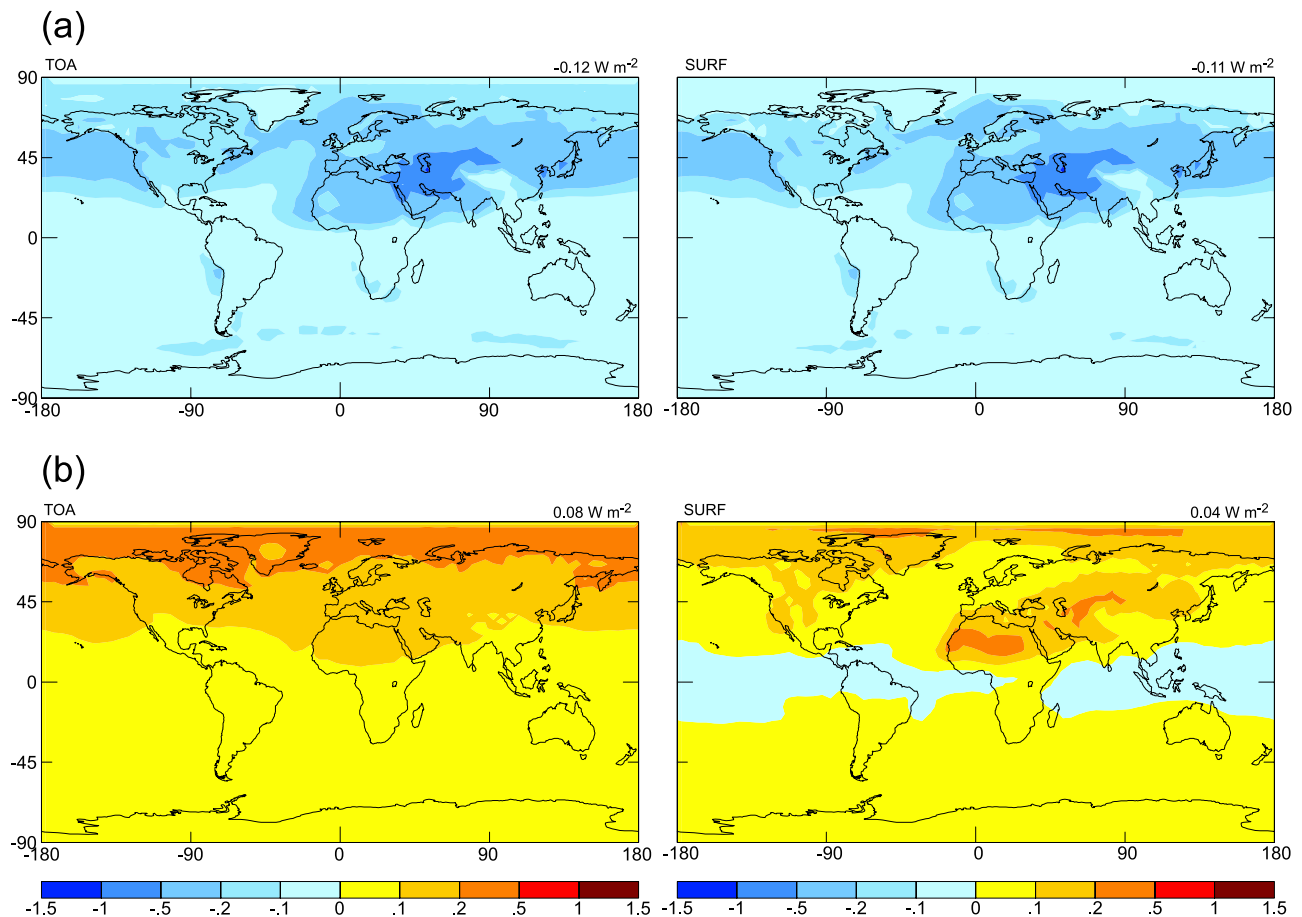


Figure 19. Differences in (a) annual mean all aerosol forcing and (b) annual mean O₃ forcing between the sensitivity study without heterogeneous reactions and the baseline simulation. (left) TOA forcing and (right) surface forcing. Global and annual mean value is indicated above each panel.

aerosols; (3) formation of sulfate in water associated with sea salt; and (4) mineral dust uptake of SO₂, HNO₃, and O₃. To examine the effects of these heterogeneous processes, we perform a sensitivity study by removing them from the baseline simulation. Note that in the sensitivity study we retain in-cloud formation of sulfate. We also retain in the sensitivity study the reaction of sea salt with HNO₃ because this reaction mainly influences nitrate forcing, the smallest forcing among all the aerosols (section 6.5.1).

[82] Table 9 lists the global and annual average burdens of some important species obtained from the baseline simulation and those in the absence of gas-aerosol chemistry. Without sea salt and dust uptake of SO₂, the burdens of SO₂ and SO₄²⁻ that is not associated with sea salt and dust increase by 23% and 28%, respectively. HNO₃ burden increases by 41%, indicating that, for the parameters assumed here, mineral dust uptake of HNO₃ is predicted to dominate the formation of HNO₃ from the hydrolysis of N₂O₅ on wet aerosol surfaces. In the absence of mineral dust uptake and NO_x removal by aerosols, the O₃ burden is predicted to increase by 16%. The ammonium burden increases by 12% as a result of more ammonium sulfate and ammonium nitrate formation, and NO₃⁻ that is not associated with dust increases by 50% with more HNO₃ available for ammonium nitrate formation and sea salt uptake.

[83] The changes in burdens of sulfate, nitrate, and O₃ have direct impacts on radiative forcing, and the changes in sulfate, HNO₃/NO₃⁻, NH₃/NH₄⁺ burdens influence water uptake by aerosols and hence also affect forcing estimates. The differences in all-aerosol and O₃ forcings between the sensitivity study without those heterogeneous reactions and the baseline simulation are shown for TOA and surface in Figure 19. The forcing by all aerosol species (mixed sulfate, nitrate, BC, OC, sea salt, dust, and aerosol water) shows about the same increase in cooling at both TOA and surface; the global and annual mean cooling is predicted to increase by 0.12 W m⁻² (or 17%) at TOA and 0.11 W m⁻² (or 2.7%) at the surface. The maximum changes of about 1 W m⁻² can be found from the Middle East to Central Asia, where dust uptake of SO₂ and HNO₃ is significant in the baseline simulation.

[84] Compared with the baseline simulation, the absence of NO_x removal by aerosols and dust uptake of O₃ increases ozone forcing at both TOA and the surface (Figure 19b). Global and annual mean TOA and surface O₃ forcings increase by 0.08 W m⁻² (or 15%) and 0.04 W m⁻² (or 57%), respectively, when they are compared to the baseline values shown in Table 8. Maximum changes at TOA are located over high albedo surfaces in the high latitudes of the NH, whereas maximum changes at the surface mainly occur in dust source regions and at high latitudes in the NH. With high aerosol concentrations and low OH abundance at

high latitudes of the NH, NO_x removal depends mainly on aerosols.

[85] Both natural and anthropogenic aerosols are included in our forcing calculations, so the effects of heterogeneous reactions on forcing estimates are compared here with the total aerosol forcing. The effects of heterogeneous reactions may become more important when anthropogenic forcing is a major concern, since the magnitude of radiative forcing by anthropogenic aerosols alone is smaller than that resulting from all aerosols.

8. Conclusions

[86] This work is an extension of the unified model of Liao *et al.* [2003] for the study of chemistry-aerosol-climate interactions by incorporating a coupled tropospheric chemistry-aerosol simulation in the GISS GCM II'. The model includes (1) a detailed simulation of tropospheric ozone- NO_x -hydrocarbon chemistry; (2) the prediction of sulfate/nitrate/ammonium/sea salt/water, black carbon, primary organic carbon, secondary organic carbon, and mineral dust aerosols; (3) heterogeneous reactions of N_2O_5 , NO_3 , NO_2 , and HO_2 on wet aerosols; (4) uptake of SO_2 and HNO_3 by sea salt; (5) uptake of SO_2 , HNO_3 and O_3 by mineral dust; and (6) effects of aerosols on gas-phase photolysis rates.

[87] The major extension of the work of Liao *et al.* [2003] is on-line simulations of sea salt and mineral dust aerosols, together with radiative forcing estimates for O_3 and aerosol species. Generation, transport, and removal of these two classes of natural aerosols are simulated as a function of particle size, with eleven size bins extending from 0.03 to 64 μm dry radius for sea salt aerosol and six bins from 0.03 to 32 μm radius for mineral dust. Comparisons with available measurements show that the model captures the global seasonal variations of sea salt and mineral dust reasonably well.

[88] The importance of heterogeneous reactions on sea salt and mineral dust to tropospheric chemistry is examined. At the surface layer, sulfate that forms from oxidation of SO_2 by O_3 within water associated with sea salt is predicted to have a global mean mixing ratio of 25.3 pptv, which is 15% of the global mean mixing ratio of nss-sulfate from direct emissions, gas-phase reaction of SO_2 with OH, and in-cloud oxidation. Accounting for heterogeneous reactions between HNO_3 and sea salt aerosol, surface layer nondust nitrate mixing ratios increase by 100–1000 pptv along polluted coastal zones. On a global mean basis, the concentrations of dust-associated sulfate and nitrate in the surface model layer are predicted to be 79 and 106 pptv, respectively. This uptake of SO_2 and HNO_3 is predicted to have a nontrivial influence on tropospheric sulfur and $\text{HNO}_3/\text{NO}_3^-$ cycles.

[89] We have used the unified model to estimate radiative forcing by aerosols and ozone. Predicted aerosol optical depths and single scattering albedos generally agree with measurements, although single-scattering albedos calculated based on currently available dust refractive indices tend to be lower than recently measured values over dust regions. We estimate the overall TOA and surface forcing by all natural and anthropogenic aerosol components, including sulfate, BC, OC, nitrate, sea salt, and dust, assuming an internal mixture of all but mineral dust. With aerosol water uptake considered, the global and annual mean values of the direct

radiative forcing by all aerosol classes are estimated to be -0.72 W m^{-2} at TOA and -4.04 W m^{-2} at the Earth's surface. As a result of absorption by BC, mineral dust, and OC, the annual mean surface forcing is predicted to reach values as high as -30 W m^{-2} . Combined forcing by tropospheric ozone and aerosols is negative at both TOA and the Earth's surface.

[90] Heterogeneous reactions on aerosols are shown to be influential in radiative forcing estimates. Through altering the burdens of aerosol sulfate and nitrate, heterogeneous reactions are predicted to change the global mean forcing of all natural and anthropogenic aerosols by 17% at TOA and 2.7% at the surface. Ignoring NO_x removal by aerosols and dust uptake of O_3 leads to an overestimate of the global mean forcing of tropospheric O_3 by 0.08 W m^{-2} at TOA and 0.04 W m^{-2} at the surface.

[91] **Acknowledgments.** This work was supported by the NASA Earth Observing System-Interdisciplinary Science Program (NASA EOS-IDS). The authors gratefully acknowledge Joe Prospero and Dennis Savoie for providing sea salt and dust measurements. We thank Brent Holben, Giuseppe Zibordi, Mary J. Bartholomew, Robert Frouin, Didier Tanre, Chuck McClain, and Arnon Karnieli for their effort in maintaining AERONET measurements used in this work. We would also like to acknowledge the Center for Advanced Computing Research at Caltech for computing resources.

References

- Adams, P. J., J. H. Seinfeld, and D. M. Koch (1999), Global concentrations of tropospheric sulfate, nitrate, and ammonium aerosol simulated in a general circulation model, *J. Geophys. Res.*, *104*, 13,791–13,824.
- Adams, P. J., J. H. Seinfeld, D. M. Koch, L. Mickley, and D. Jacob (2001), General circulation model assessment of direct radiative forcing by the sulfate-nitrate-ammonium-water inorganic aerosol system, *J. Geophys. Res.*, *106*, 1097–1111.
- Anderson, T. L., D. S. Covert, J. D. Wheeler, J. M. Harris, K. D. Perry, B. E. Trost, D. J. Jaffe, and J. A. Ogren (1999), Aerosol backscatter fraction and single scattering albedo: Measured values and uncertainties at a coastal station in the Pacific Northwest, *J. Geophys. Res.*, *104*, 26,793–26,807.
- Andreas, E. L. (1998), A new sea spray generation function for wind speeds up to 32 m s^{-1} , *J. Phys. Oceanogr.*, *28*, 2175–2184.
- Bauer, S. E., Y. Balkanski, M. Schulz, D. A. Hauglustaine, and F. Dentener (2004), Global modeling of heterogeneous chemistry on mineral aerosol surfaces: The influence on tropospheric ozone chemistry and comparison to observations, *J. Geophys. Res.*, *109*, D02304, doi:10.1029/2003JD003868.
- Berntsen, T. K., G. Myhre, F. Stordal, and I. S. A. Isaksen (2000), Time evolution of tropospheric ozone and its radiative forcing, *J. Geophys. Res.*, *105*, 8915–8930.
- Bodhaine, B. A. (1995), Aerosol absorption measurements at Barrow, Mauna Loa, and the south pole, *J. Geophys. Res.*, *100*, 8967–8975.
- Bond, T. C., T. L. Anderson, and D. Campbell (1999), Calibration and intercomparison of filter-based measurements of visible light absorption by aerosols, *Aerosol Sci. Technol.*, *30*, 582–600.
- Boucher, O., and T. L. Anderson (1995), General circulation model assessment of the sensitivity of direct climate forcing by anthropogenic sulfate aerosols to aerosol size and chemistry, *J. Geophys. Res.*, *100*, 26,117–26,134.
- Brasseur, G. P., J. H. Orlando, and G. S. Tyndall (1999), *Atmospheric Chemistry and Global Change*, Oxford Univ. Press, New York.
- Bush, B. C., and F. P. J. Valero (2003), Surface aerosol radiative forcing at Gosan during the ACE-Asia campaign, *J. Geophys. Res.*, *108*(D23), 8660, doi:10.1029/2002JD003233.
- Carlson, T. N., and S. G. Benjamin (1980), Radiative heating rates for Saharan Dust, *J. Atmos. Sci.*, *37*, 193–213.
- Carrico, C. M., M. J. Rood, J. A. Ogren, C. Neusüß, A. Wiedensohler, and J. Heintzenberg (2000), Aerosol optical properties at Sagres, Portugal during ACE-2, *Tellus, Ser. B*, *52*, 694–751.
- Chalita, S., D. A. Hauglustaine, H. LeTreut, and J. F. Muller (1996), Radiative forcing due to increased tropospheric ozone concentrations, *Atmos. Environ.*, *30*, 1641–1646.
- Chameides, W. L., and A. W. Stelson (1993), Aqueous-phase chemical processes in deliquescent sea-salt aerosols: A mechanism that couples

- the atmospheric cycles of S and sea salt, *J. Geophys. Res.*, *97*, 20,565–20,580.
- Chuang, P. Y., R. M. Duvall, M. S. Bae, A. Jefferson, J. J. Schauer, H. Yang, J. Z. Yu, and J. Kim (2003), Observations of elemental carbon and absorption during ACE-Asia and implications for aerosol radiative properties and climate forcing, *J. Geophys. Res.*, *108*(D23), 8634, doi:10.1029/2002JD003254.
- Chung, S. H., and J. H. Seinfeld (2002), Global distribution and climate forcing of carbonaceous aerosols, *J. Geophys. Res.*, *107*(D19), 4407, doi:10.1029/2001JD001397.
- Clarke, A. D. (1989), Aerosol light absorption by soot in remote environments, *Aerosol. Sci. Technol.*, *10*, 161–171.
- Cooke, W. F., C. Liou, H. Cachier, and J. Feichter (1999), Construction of a $1^\circ \times 1^\circ$ fossil fuel emission data set for carbonaceous aerosol and implementation and radiative impact in the ECHAM4 model, *J. Geophys. Res.*, *104*, 22,137–22,162.
- d'Almeida, G. A., P. Koepke, and E. P. Shettle (1991), *Atmospheric Aerosols: Global Climatology and Radiative Characteristics*, A. Deepak, Hampton, Va.
- Dana, M. T., and J. M. Hales (1976), Statistical aspects of the washout of polydisperse aerosols, *Atmos. Environ.*, *10*, 45–50.
- Del Genio, A. D., and M.-S. Yao (1993), Efficient cumulus parameterization for long-term climate studies: The GISS scheme, in *The Representation of Cumulus Convection in Numerical Models*, Monogr. 46, edited by K. A. Emanuel and D. J. Raymond, pp. 181–184, Am. Meteorol. Soc., Boston, Mass.
- Del Genio, A. D., M.-S. Yao, W. Kovari, and K. K.-W. Lo (1996), A prognostic cloud water parameterization for global climate models, *J. Clim.*, *9*, 270–304.
- Dentener, F. J., and P. J. Crutzen (1993), Reaction of N_2O_5 on tropospheric aerosols: Impact on the global distributions of NO_x , O_3 , and OH, *J. Geophys. Res.*, *98*, 7149–7163.
- Dentener, F. J., G. R. Carmichael, Y. Zhang, J. Lelieveld, and P. J. Crutzen (1996), Role of mineral aerosol as a reactive surface in the global troposphere, *J. Geophys. Res.*, *101*, 22,869–22,889.
- Erickson, D. J., C. Seuzaret, W. C. Keene, and S. L. Gong (1999), A general circulation model based calculation of HCl and ClNO_2 production from sea salt dechlorination: Reactive chlorine emissions inventory, *J. Geophys. Res.*, *104*, 8347–8372.
- Feichter, J., U. Lohmann, and I. Schult (1997), The atmospheric sulfur cycle in ECHAM-4 and its impact on the shortwave radiation, *Clim. Dyn.*, *13*, 235–246.
- Fenter, F. F., F. Caloz, and M. J. Rossi (1995), Experimental evidence for efficient dry deposition of nitric acid on calcite, *Atmos. Environ.*, *29*, 3365–3372.
- Ferman, M. A., G. T. Wolff, and N. A. Kelly (1981), The nature and sources of haze in the Shenandoah Valley/Blue Ridge Mountain area, *J. Air Pollut. Control Assoc.*, *31*, 1074–1082.
- Fitzgerald, J. M. (1991), Marine aerosols: A review, *Atmos. Environ., Part A*, *25*, 533–545.
- Galy-Lacaux, C., and A. I. Modi (1998), Precipitation chemistry in the Sahelian savanna of Niger Africa, *J. Atmos. Chem.*, *30*, 319–343.
- Galy-Lacaux, C., G. R. Carmichael, C. H. Song, J. P. Lacaux, H. Al Ourabi, and A. I. Modi (2001), Heterogeneous processes involving nitrogenous compounds and Saharan dust inferred from measurements and model calculations, *J. Geophys. Res.*, *106*, 12,559–12,578.
- Gerber, H. E. (1985), Relative-humidity parameterization of the Navy aerosol model (NAM), *NRL Rep. 8956*, Natl. Res. Lab., Washington, D. C.
- Ghan, S., N. Laulainen, R. Easter, R. Wagener, S. Nemesure, E. Chapman, Y. Zhang, and R. Leung (2001), Evaluation of aerosol direct radiative forcing in MIRAG, *J. Geophys. Res.*, *106*, 5295–5316.
- Gillette, D. (1978), A wind tunnel simulation of the erosion of soil: Effect of soil texture, sandblasting, wind speed, and soil consolidation on dust production, *Atmos. Environ.*, *12*, 1735–1743.
- Ginoux, P., M. Chin, I. Tegen, J. M. Prospero, B. Holben, O. Dubovik, and S. J. Lin (2001), Sources and distributions of dust aerosols simulated with the GOCART model, *J. Geophys. Res.*, *106*, 20,255–20,273.
- Gong, S. L., L. A. Barrie, J. M. Prospero, D. L. Savoie, G. P. Ayers, J. P. Blanchet, and L. Spacek (1997), Modeling sea-salt aerosols in the atmosphere: 2. Atmospheric concentrations and fluxes, *J. Geophys. Res.*, *102*, 3819–3830.
- Goodman, A. L., G. M. Underwood, and V. H. Grassian (2000), A laboratory study of the heterogeneous reaction of nitric acid on calcium carbonate particles, *J. Geophys. Res.*, *105*, 29,053–29,064.
- Grini, A., G. Myhre, J. K. Sundet, and I. S. A. Isaksen (2002), Modeling the annual cycle of sea salt in the global 3D model Oslo CTM2: Concentrations, fluxes, and radiative impact, *J. Clim.*, *15*, 1717–1730.
- Guelle, W., M. Schulz, Y. Balkanski, and F. Dentener (2001), Influence of the source formulation on modeling the atmospheric global distribution of sea salt aerosol, *J. Geophys. Res.*, *106*, 27,509–27,524.
- Gurciullo, C., B. Lerner, H. Sievering, and S. N. Pandis (1999), Heterogeneous sulfate production in the remote marine environment: Cloud processing and sea-salt particle contributions, *J. Geophys. Res.*, *104*, 21,719–21,731.
- Hanisch, F., and J. N. Crowley (2001), Heterogeneous reactivity of gaseous nitric acid on Al_2O_3 , CaCO_3 , and atmospheric dust samples: A Knudsen cell study, *J. Phys. Chem. A*, *105*, 3096–3106.
- Hansen, J., G. Russell, D. Rind, P. Stone, A. Lacis, S. Lebedeff, R. Ruedy, and L. Travis (1983), Efficient three-dimensional global models for climate studies: Models I and II, *Mon. Weather Rev.*, *111*, 609–662.
- Hauglustaine, D. A., and G. P. Brasseur (2001), Evolution of tropospheric ozone under anthropogenic activities and associated radiative forcing of climate, *J. Geophys. Res.*, *106*, 32,337–32,360.
- Hegg, D. A., J. Livingston, P. V. Hobbs, T. Novakov, and P. Russell (1997), Chemical apportionment of aerosol column optical depth off the mid-Atlantic coast of the United States, *J. Geophys. Res.*, *102*, 25,293–25,303.
- Heintzenberg, J. (1982), Measurement of light absorption and elementary carbon in atmospheric aerosol samples from remote locations, in *Particulate Carbon: Atmospheric Life Cycle*, edited by G. T. Wolff and R. L. Klimisch, pp. 371–373, Plenum, New York.
- Heintzenberg, J., and C. Leck (1994), Seasonal variation of the atmospheric aerosol near the top of the marine boundary layer over Pitsbergen related to the arctic sulfur cycle, *Tellus, Ser. B*, *46*, 52–67.
- Heintzenberg, J., R. J. Charlson, A. D. Clarke, C. Liou, V. Ramaswamy, K. P. Shine, M. Wendisch, and G. Helas (1997), Measurements and modeling of aerosol single-scattering albedo: Progress, problems, and prospects, *Contrib. Atmos. Phys.*, *70*, 249–263.
- Holben, B. N., et al. (1998), AERONET - A federated instrument network and data archive for aerosol characterization, *Remote Sens. Environ.*, *66*, 1–16.
- Holben, B. N., et al. (2001), An emerging ground-based aerosol climatology: Aerosol optical depth from AERONET, *J. Geophys. Res.*, *106*, 12,067–12,097.
- Jacob, D. J. (2000), Heterogeneous chemistry and tropospheric ozone, *Atmos.*, 2131–2159.
- Jacobson, M. Z. (2000), A physically based treatment of elemental carbon optics: Implication for global direct forcing of aerosols, *Geophys. Res. Lett.*, *27*, 217–220.
- Jacobson, M. Z. (2001), Global direct radiative forcing due to multicomponent anthropogenic and natural aerosols, *J. Geophys. Res.*, *106*, 1551–1568.
- Jacobson, M. Z., and R. P. Turco (1994), SMVGEAR - A sparse-matrix, vectorized GEAR code for atmospheric models, *Atmos. Environ.*, *28*, 273–284.
- Japar, S. M., W. W. Brachaczek, R. A. Gorse Jr., J. M. Norbeck, and W. R. Pierson (1986), The contribution of elemental carbon to the optical properties of rural atmospheric aerosols, *Atmos. Environ.*, *20*, 1281–1289.
- Kalma, J. D., J. G. Speight, and R. J. Wason (1988), Potential wind erosion in Australia: A continental perspective, *J. Climatol.*, *8*, 411–428.
- Kiehl, J. T., T. L. Schneider, P. J. Rasch, M. C. Barth, and J. Wong (2000), Radiative forcing due to sulfate aerosols from simulations with the National Center for Atmospheric Research Community Climate Model, Version 3, *J. Geophys. Res.*, *105*, 1441–1457.
- Koch, D. M. (2001), Transport and direct radiative forcing of carbonaceous and sulfate aerosols in the GISS GCM, *J. Geophys. Res.*, *106*, 20,311–20,332.
- Koch, D. M., D. Jacob, I. Tegen, D. Rind, and M. Chin (1999), Tropospheric sulfur simulation and sulfate direct radiative forcing in the Goddard Institute for Space Studies general circulation model, *J. Geophys. Res.*, *104*, 23,799–23,822.
- Lacis, A. A., and J. E. Hansen (1974), A parameterization for the absorption of solar radiation in the earth's atmosphere, *J. Aerosol Sci.*, *31*, 118–133.
- Lacis, A. A., and M. I. Mishchenko (1995), Climate forcing, climate sensitivity, and climate response: A radiative modeling perspective on atmospheric aerosols, in *Aerosol Forcing of Climate*, edited by R. J. Charlson and J. Heintzenberg, pp. 11–42, John Wiley, Hoboken, N. J.
- Lacis, A. A., and V. Oinas (1991), A description of the correlated k -distribution method for modeling nongray gaseous absorption, thermal emission, and multiple-scattering in vertically inhomogeneous atmospheres, *J. Geophys. Res.*, *96*, 9027–9063.
- Laskin, A., D. J. Gaspar, W. Wang, S. W. Hunt, J. P. Cowin, S. D. Colson, and B. J. Finlayson-Pitts (2003), Reactions at interfaces as a source of sulfate formation in sea-salt particles, *Science*, *301*, 340–344.
- Lestari, P., A. K. Oskouie, and K. E. Noll (2003), Size distribution and dry deposition of particulate mass, sulfate, and nitrate in an urban area, *Atmos. Environ.*, *37*, 2507–2516.

- Liao, H., and J. H. Seinfeld (1998), Radiative forcing by mineral dust aerosols: Sensitivity to key variables, *J. Geophys. Res.*, *103*, 31,637–31,645.
- Liao, H., P. J. Adams, S. H. Chung, J. H. Seinfeld, L. J. Mickley, and D. J. Jacob (2003), Interactions between tropospheric chemistry and aerosols in a unified general circulation model, *J. Geophys. Res.*, *108*(D1), 4001, doi:10.1029/2001JD001260.
- Lurmann, F. W., A. S. Wexler, S. N. Pandis, S. Musarra, N. Kumar, and J. H. Seinfeld (1997), Modeling urban and regional aerosols-II. Application to California's south coast air basin, *Atmos. Environ.*, *31*, 2695–2715.
- Mari, C., K. Suhre, R. Rosset, T. S. Bates, B. J. Huebert, A. R. Bandy, D. C. Thornton, and S. Businger (1999), One-dimensional modeling of sulfur species during the First Aerosol Characterization Experiment (ACE 1) Lagrangian B, *J. Geophys. Res.*, *104*, 21,733–21,749.
- Merrill, J. T., M. Uematsu, and R. Bleck (1989), Meteorological analysis of long-range transport of mineral aerosols over the North Pacific, *J. Geophys. Res.*, *94*, 8584–8598.
- Mickley, L. J., P. Murti, D. Jacob, J. Logan, and D. Rind (1999), Radiative forcing from tropospheric ozone calculated with a unified chemistry-climate model, *J. Geophys. Res.*, *104*, 30,153–30,172.
- Monahan, E. C., D. E. Spiel, and K. L. Davidson (1986), A model of marine aerosol generation via whitecaps and wave disruption, in *Oceanic Whitecaps and Their Role in Air-Sea Exchange*, edited by E. C. Monahan and G. MacNiocaill, pp. 167–174, D. Reidel, Norwell, Mass.
- Nenes, A., C. Pilinits, and S. N. Pandis (1998), Isorropia: A new thermodynamic equilibrium model for multiphase multicomponent inorganic aerosols, *Aquat. Geochem.*, *4*, 123–152.
- Ogren, J. A., R. J. Charlson, D. S. Covert, T. L. Anderson, and M. J. Rood (1999), Measurements of aerosol single-scattering albedo: Implications of its observed variability on estimates of aerosol radiative forcing, paper presented at CNES Workshop on Reduction of Errors in Aerosol Forcing of Climate, Meribel, France, 19–22 Jan.
- Olson, J. (1992), World ecosystems (WE1.4): Digital raster data on a 10 minute geographic 1080 × 2160 grid, in *Global Ecosystems Database, Version 1.0: Disc A*, Natl. Geophys. Data Cent., Natl. Oceanic and Atmos. Admin., Boulder, Colo.
- Pandis, S. N., A. S. Wexler, and J. H. Seinfeld (1993), Secondary organic aerosol formation and transport-II. Predicting the ambient secondary organic aerosol size distribution, *Atmos. Environ.*, *27*, 2403–2416.
- Parungo, F., et al. (1995), Asian dust storms and their effects on radiation and climate, *Tech. Rep. STC 2906*, Natl. Oceanic and Atmos. Admin., Silver Spring, Md.
- Penner, J. E., C. C. Chuang, and K. Grant (1998), Climate forcing by carbonaceous and sulfate aerosols, *Clim. Dyn.*, 839–851.
- Perlwitz, J., I. Tegen, and R. L. Miller (2001), Interactive soil dust aerosol model in the GISS GCM: 1. Sensitivity of the soil dust cycle to radiative properties of soil dust aerosols, *J. Geophys. Res.*, *106*, 18,167–18,192.
- Prospero, J. M. (1996), The atmospheric transport of particles to the ocean, in *Particle Flux in the Ocean*, edited by V. Ittekkott et al., John Wiley, Hoboken, N. J.
- Prospero, J. M., D. L. Savoie, and R. Arimoto (2003), Long-term record of nss-sulfate and nitrate in aerosols on Midway Island, 1981–2000: Evidence of increased (now decreasing?) anthropogenic emissions from Asia, *J. Geophys. Res.*, *108*(D1), 4019, doi:10.1029/2001JD001524.
- Pye, K. (1987), *Aeolian Dust Particles and Dust Deposits*, Academic, San Diego, Calif.
- Quinn, P. K., V. N. Kapustin, T. S. Bates, and D. S. Covert (1998), Aerosol optical properties in the marine boundary layer during the First Aerosol Characterization Experiment (ACE 1) and the underlying chemical and physical aerosol properties, *J. Geophys. Res.*, *103*, 16,547–16,563.
- Quinn, P. K., D. J. Coffman, T. S. Bates, T. L. Miller, J. E. Johnson, K. Voss, E. J. Welton, and C. Neususs (2001), Dominant aerosol chemical components and their contribution to extinction during the Aerosols99 cruise across the Atlantic, *J. Geophys. Res.*, *106*, 20,783–20,809.
- Quinn, P. K., T. L. Miller, T. S. Bates, J. A. Ogren, E. Andrews, and G. E. Shaw (2002), A 3-year record of simultaneously measured aerosol chemical and optical properties at Barrow Alaska, *J. Geophys. Res.*, *107*(D11), 4130, doi:10.1029/2001JD001248.
- Reid, J. S., P. V. Hobbs, R. J. Ferek, D. R. Blake, J. V. Martins, M. R. Dunlap, and C. Liou (1998), Physical, chemical, and optical properties of regional hazes dominated by smoke in Brazil, *J. Geophys. Res.*, *103*, 32,059–32,080.
- Rhoads, K. P., P. Kelley, R. R. Dickerson, T. P. Carsey, M. Farmer, D. L. Savoie, and J. M. Prospero (1997), Composition of the troposphere over the Indian Ocean during the monsoonal transition, *J. Geophys. Res.*, *102*, 18,981–18,995.
- Rind, D., and J. Lerner (1996), The use of on-line tracers as a diagnostic tool in general circulation model development: 1. Horizontal and vertical transport in the troposphere, *J. Geophys. Res.*, *101*, 12,667–12,683.
- Rind, D., J. Lerner, K. Shah, and R. Suozzo (1999), Use of on-line tracers as a diagnostic tool in general circulation model development: 2. Transport between the troposphere and stratosphere, *J. Geophys. Res.*, *104*, 9151–9167.
- Robinson, R. A., and R. H. Stokes (1965), *Electrolyte Solutions*, 2nd ed., Butterworth-Heinemann, Woburn, Mass.
- Roelofs, G.-J., and J. Lelieveld (2000), Tropospheric ozone simulation with a chemistry general circulation model: Influence of higher hydrocarbon chemistry, *J. Geophys. Res.*, *105*, 22,697–22,712.
- Satheesh, S. K., and V. Ramanathan (2000), Large differences in tropical aerosol forcing at the top of atmosphere and Earth's surface, *Nature*, *405*, 60–63.
- Savoie, D. L., R. Arimoto, W. C. Keene, J. M. Prospero, R. A. Duce, and J. N. Galloway (2002), Marine biogenic and anthropogenic contributions to non-sea-salt sulfate in the marine boundary layer over the North Atlantic Ocean, *J. Geophys. Res.*, *107*(D18), 4356, doi:10.1029/2001JD000970.
- Schult, I., J. Feichter, and W. F. Cooke (1997), Effect of black carbon and sulfate aerosols on the global radiation budget, *J. Geophys. Res.*, *102*, 30,107–30,117.
- Schwartz, S. E. (1986), Mass-transport considerations pertinent to aqueous-phase reactions of gases in liquid-water clouds, in *Chemistry of Multiphase Atmospheric Systems*, edited by W. Jaeschke, pp. 415–471, Springer-Verlag, New York.
- Seinfeld, J. H., and S. N. Pandis (1998), *Atmospheric Chemistry and Physics*, John Wiley, Hoboken, N. J.
- Shindell, D. T., J. L. Grenfell, D. Rind, V. Grewe, and C. Price (2001), Chemistry-climate interactions in the Goddard Institute for Space Studies general circulation model: 1. Tropospheric chemistry model description and evaluation, *J. Geophys. Res.*, *106*, 8047–8075.
- Sievering, H., J. Boatman, J. Galloway, W. Keene, Y. Kim, M. Luria, and J. Ray (1991), Heterogeneous sulfur conversion in sea-salt aerosol particles: The role of aerosol water content and size distribution, *Atmos. Environ.*, *25*, 1479–1487.
- Sievering, H., J. Boatman, E. Gorman, Y. Kim, L. Anderson, G. Ennis, M. Luria, and S. Pandis (1992), Removal of sulfur oxidation in sea-salt aerosols, *Nature*, *306*, 571–573.
- Sirokko, F., and M. Sarnheim (1989), Wind-borne deposits in the northwestern Indian Ocean: Record of Holocene sediments versus satellite data, in *Paleoclimatology and Paleometeorology: Modern and Past Patterns of Global Atmospheric Transport*, edited by M. Leinen and M. Sarnheim, pp. 401–433, Kluwer Acad., Norwell, Mass.
- Sloane, C. S. (1983), Optical properties of aerosols: Comparison of measurements with model calculations, *Atmos. Environ.*, *17*, 409–416.
- Smith, K. H., and N. M. Harrison (1998), The sea spray generation function, *J. Aerosol Sci.*, *29*, suppl. 1, S189–S190.
- Song, C. H., and G. R. Carmichael (2001), A three-dimensional modeling investigation of the evolution processes of dust and sea-salt particles in east Asia, *J. Geophys. Res.*, *106*, 18,131–18,154.
- Stevenson, D. S., C. E. Johnson, W. J. Collins, R. G. Derwent, K. P. Shine, and J. M. Edwards (1998), Evolution of tropospheric ozone radiative forcing, *Geophys. Res. Lett.*, *25*, 3819–3822.
- Swap, R., S. Ulanski, M. Cobbett, and M. Garstang (1996), Temporal and spatial characteristics of Saharan dust outbreaks, *J. Geophys. Res.*, *101*, 4205–4220.
- Tabazadeh, A., M. Z. Jacobson, H. B. Singh, O. B. Toon, J. S. Linn, R. B. Chatfield, A. N. Thakur, R. W. Talbot, and J. E. Dibb (1998), Nitric acid scavenging by mineral and biomass burning aerosols, *Geophys. Res. Lett.*, *25*, 4185–4188.
- Takemura, T., H. Okamoto, Y. Maruyama, A. Numaguti, A. Higurashi, and T. Nakajima (2000), Global three-dimensional simulation of aerosol optical thickness distribution of various origins, *J. Geophys. Res.*, *105*, 17,853–17,873.
- Takemura, T., T. Nakajima, O. Dubovik, B. N. Holben, and S. Kinne (2002), Single-scattering albedo and radiative forcing of various aerosol species with a global three-dimensional model, *J. Clim.*, *15*, 333–352.
- Tegen, I., and I. Fung (1995), Contribution to the atmospheric mineral aerosol load from land-surface modification, *J. Geophys. Res.*, *100*, 18,707–18,726.
- Tegen, I., and A. A. Lacis (1996), Modeling of particle size distribution and its influence on the radiative properties of mineral dust aerosol, *J. Geophys. Res.*, *101*, 19,237–19,244.
- Tegen, I., P. Hollrig, M. Chin, I. Fung, D. Jacob, and J. Penner (1997), Contribution of different aerosol species to the global aerosol extinction optical thickness: Estimates from model results, *J. Geophys. Res.*, *102*, 23,895–23,915.
- Tegen, I., S. P. Harrison, K. Kohfeld, I. C. Prentice, M. Coe, and M. Heimann (2002), Impact of vegetation and preferential source areas

- on global dust aerosol: Results from a model study, *J. Geophys. Res.*, *107*(D21), 4576, doi:10.1029/2001JD000963.
- Toon, O. B., J. B. Pollack, and B. N. Khare (1976), The optical constants of several atmospheric aerosol species: Ammonium sulfate, aluminum oxide, and sodium chloride, *J. Geophys. Res.*, *81*, 5733–5748.
- Underwood, G. M., P. Li, H. Al-Abadleh, and V. H. Grassian (2001), A Knudsen cell study of the heterogeneous reactivity of nitric acid on oxide and mineral dust particles, *J. Phys. Chem.*, 6609–6620.
- van Dorland, R., F. J. Dentener, and J. Lelieveld (1997), Radiative forcing due to tropospheric ozone and sulfate aerosols, *J. Geophys. Res.*, *102*, 28,079–28,100.
- Volz, F. E. (1972), Infrared absorption by atmospheric aerosol substances, *J. Geophys. Res.*, *77*, 1017–1031.
- Wesely, M. L. (1989), Parameterization of surface resistances to gaseous dry deposition in regional-scale numerical models, *Atmos. Environ.*, *23*, 1293–1304.
- Wild, O., X. Zhu, and M. J. Prather (2000), Fast-J: Accurate simulation of in- and below-cloud photolysis in tropospheric chemical models, *J. Atmos. Chem.*, *37*, 245–282.
- Wilson, M. F., and A. Henderson-Sellers (1985), A global archive of land cover and soils data for use in general circulation climate models, *J. Climatol.*, *5*, 119–143.
- Woodward, S. (2001), Modeling the atmospheric life cycle and radiative impact of mineral dust in the Hadley Centre climate model, *J. Geophys. Res.*, *106*, 18,155–18,166.
- Zender, C. S., H. Bian, and D. Newman (2003), Mineral Dust Entrainment and Deposition (DEAD) model: Description and 1990s dust climatology, *J. Geophys. Res.*, *108*(D14), 4416, doi:10.1029/2002JD002775.
- Zhang, Y., Y. Sunwoo, V. Kotamarthi, and G. R. Carmichael (1994), Photochemical oxidant processes in the presence of dust: An evaluation of the impact of dust on particulate nitrate and ozone formation, *J. Appl. Meteorol.*, *33*, 813–824.

P. J. Adams, Department of Civil and Environmental Engineering and Department of Engineering and Public Policy, Carnegie Mellon University, Pittsburgh, PA 15213, USA.

H. Liao and J. H. Seinfeld, Division of Engineering and Applied Science and Department of Chemical Engineering, California Institute of Technology, Pasadena, CA 91125, USA. (seinfeld@caltech.edu)

L. J. Mickley, Department of Earth and Planetary Sciences and Division of Engineering and Applied Sciences, Harvard University, Cambridge, MA 02138, USA.